The contribution of in-situ and ex-situ star formation in early-type galaxies: MaNGA versus IllustrisTNG

Cannarozzo, C.; Leauthaud, A.; Oyarzún, G.A.; Nipoti, C.; Diemer, B.; Huang, S.; ... ; Bundy, K.

Citation

Cannarozzo, C., Leauthaud, A., Oyarzún, G. A., Nipoti, C., Diemer, B., Huang, S., ... Bundy, K. (2023). The contribution of in-situ and ex-situ star formation in early-type galaxies: MaNGA versus IllustrisTNG. *Monthly Notices Of The Royal Astronomical Society*. doi:10.1093/mnras/stac3023

MNRAS **000**, 1–20 (2022) Preprint October 18, 2022 Compiled using MNRAS LaTeX style file v3.0

The Contribution of In-situ and Ex-situ Star Formation in Early-Type Galaxies: MaNGA versus IllustrisTNG

Carlo Cannarozzo[1,2,3] *, Alexie Leauthaud[4], Grecco A. Oyarzún[4], Carlo Nipoti[2], Benedikt Diemer[5], Song Huang[6], Vicente Rodriguez-Gomez[7], Alessandro Sonnenfeld[8], and Kevin Bundy[4,9]

[1] *Instituto de Astronomía, Universidad Nacional Autónoma de México, A. P. 70-264, 04510 CDMX, México*
[2] *Dipartimento di Fisica e Astronomia "Augusto Righi", Alma Mater Studiorum Università di Bologna, via Piero Gobetti 93/2, I-40129 Bologna, Italy*
[3] *INAF - Osservatorio di Astrofisica e Scienza dello Spazio di Bologna, Via Piero Gobetti 93/3, I-40129 Bologna, Italy*
[4] *Department of Astronomy and Astrophysics, UCO/Lick Observatory, University of California, 1156 High Street, Santa Cruz, CA 95064, USA*
[5] *Department of Astronomy, University of Maryland, College Park, MD 20742, USA*
[6] *Department of Astrophysical Sciences, Princeton University, 4 Ivy Lane, Princeton, NJ 08544, USA*
[7] *Instituto de Radioastronomía y Astrofísica, Universidad Nacional Autónoma de México, A. P. 72-3, 58089 Morelia, Mexico*
[8] *Leiden Observatory, Leiden University, Niels Bohrweg 2, 2333 CA Leiden, The Netherlands*
[9] *UCO/Lick Observatory, University of California, Santa Cruz, 1156 High Street, Santa Cruz, CA 95064, USA*

Accepted 2022 October 14. Received 2022 October 13; in original form 2022 May 02

ABSTRACT

We compare stellar mass surface density, metallicity, age, and line-of-sight velocity dispersion profiles in massive ($M_* \geq 10^{10.5}\,\mathrm{M}_\odot$) present-day early-type galaxies (ETGs) from the MaNGA survey with simulated galaxies from the TNG100 simulation of the IllustrisTNG suite. We find an excellent agreement between the stellar mass surface density profiles of MaNGA and TNG100 ETGs, both in shape and normalisation. Moreover, TNG100 reproduces the shapes of the profiles of stellar metallicity and age, as well as the normalisation of velocity dispersion distributions of MaNGA ETGs. We generally also find good agreement when comparing the stellar profiles of central and satellite galaxies between MaNGA and TNG100. An exception is the velocity dispersion profiles of very massive ($M_* \gtrsim 10^{11.5}\,\mathrm{M}_\odot$) central galaxies, which, on average, are significantly higher in TNG100 than in MaNGA ($\approx 50\,\mathrm{km\,s^{-1}}$). We study the radial profiles of *in-situ* and *ex-situ* stars in TNG100 and discuss the extent to which each population contributes to the observed MaNGA profiles. Our analysis lends significant support to the idea that high-mass ($M_* \gtrsim 10^{11}\,\mathrm{M}_\odot$) ETGs in the present-day Universe are the result of a merger-driven evolution marked by major mergers that tend to homogenise the stellar populations of the progenitors in the merger remnant.

Key words: galaxies: elliptical and lenticular, cD – galaxies: evolution – galaxies: formation – galaxies: interactions – galaxies: stellar content – galaxies: structure

1 INTRODUCTION

In the standard cosmological framework, the formation and evolution of galaxies is thought to be driven by mergers and the accretion of material from the intergalactic medium (e.g. Cimatti et al. 2019). In particular, for the assembly of massive early-type galaxies (ETGs), a *two-phase formation scenario* has been proposed (e.g., Naab et al. 2009; Oser et al. 2010; Hilz et al. 2013). In the first phase of this formation process ($z \gtrsim 2$), ETGs are built from stars formed *in situ*, i.e. within the same galaxy, while later, as a consequence of minor and major mergers, ETGs grow mainly by the accretion of stars formed *ex situ*, i.e. in other galaxies.

A natural outcome of mergers experienced by ETGs is the evolution of scaling relations (e.g. Cimatti et al. 2019), i.e. the observed empirical correlations between global galaxy properties, such as those relating luminosity (or mass) with stellar velocity dispersion (Faber & Jackson 1976), size (Kormendy 1977), or both (the so-called fundamental plane; Djorgovski & Davis 1987; Dressler et al. 1987). The improvement of instrumentation technology together with increasing statistics in recent surveys has enabled studies of those relations at different redshifts. Indeed, massive ETGs at high redshift are found to be compact, with an effective radius R_e smaller than that of galaxies of similar stellar mass in the present-day Universe (e.g., Ferguson et al. 2004; van der Wel et al. 2014; Damjanov et al. 2019). Also the stellar mass–central velocity dispersion relation (M_*–σ_e) evolves: on average, for a given stellar mass, the lower

*E-mail: ccannarozzo@astro.unam.mx

the redshift, the lower the velocity dispersion (e.g., van de Sande et al. 2013; Belli et al. 2014, 2017; Tanaka et al. 2019; Cannarozzo et al. 2020).

Mergers and accretion not only affect global galaxy properties, but also the internal distributions of stellar properties. The spatial distributions of metallicity, chemical abundances, age and other properties of stellar populations in a galaxy enclose information on the evolutionary processes that have occurred across cosmic time. One possible way to investigate how progenitor stellar populations come together to form present day ETGs is to perform galaxy-scale high-resolution simulations, an approach recently adopted, for instance, by Nipoti et al. (2020) to study the effect of mergers on the internal distributions of the stellar initial mass function (IMF) and the velocity dispersion in ETGs. A second approach is the study of the evolution of stellar population properties using hydrodynamical cosmological simulations. For example, Oser et al. (2012), exploiting a set of fourty zoom-in hydrodynamical simulations of individual halos presented in Oser et al. (2010), and Rodriguez-Gomez et al. (2016) using the Illustris (Vogelsberger et al. 2014b,a; Genel et al. 2014; Sijacki et al. 2015) simulations, studied the radial distributions of in-situ and ex-situ stars in ETGs. With a similar approach, Barber et al. (2019) studied IMF radial gradients in ETGs drawn from the Evolution and Assembly of GaLaxies and their Environments (EAGLE; Schaye et al. 2015; Crain et al. 2015; McAlpine et al. 2016) cosmological simulations.

The presence of initial gradients in stellar metallicity are thoughts to be established during the first episodes of star formation (e.g., Larson 1974; Thomas et al. 2005) with metallicity profiles that decrease towards the external regions of galaxies, but with fairly flat stellar age profiles. As shown in Hirschmann et al. (2015) using a set of ten high-resolution cosmological zoom simulations presented in Hirschmann et al. (2013), as well as in Cook et al. (2016) taking data from Illustris, the large number of mergers and interactions that occur in galaxies then tend to flatten metallicity profiles and almost flatten (or lead to slightly positive) age gradients both because of the mixing of stars with different metallicities and the accumulation of old stellar populations in the outer regions. On the contrary, galaxies with few mergers may retain their original negative metallicity profiles with metal-poor regions dominating in the outskirts of galaxies (e.g., Kobayashi 2004; Pipino et al. 2010; Taylor & Kobayashi 2017).

In the last few decades, integral field spectroscopy (IFS) has formed the basis of many surveys: SAURON (Spectroscopic Areal Unit for Research on Optical Nebulae; Bacon et al. 2001; de Zeeuw et al. 2002), ATLAS$^{\rm 3D}$ (Cappellari et al. 2011), CALIFA (Calar Alto Legacy Integral Field Array survey; Sánchez et al. 2016), SAMI (Sydney-Australian-Astronomical-Observatory Multi-object Integral-Field Spectrograph Croom et al. 2012; Bryant et al. 2015), MASSIVE (Ma et al. 2014) and MaNGA (Mapping Nearby Galaxies at Apache Point Observatory; Bundy et al. 2015). These spatially-resolved surveys allow in depth studies of the properties of stellar populations in individual objects, therefore not limiting analyses only to the study of gradients, but revealing the 2D spatial distribution over the entire galaxy on the plane of the sky. By analysing a set of ETGs with $\log(M_*/\mathrm{M}_\odot) > 10.3$ in SAURON, Kuntschner et al. (2010) found that stellar metallicity gradients become shallower with increasing stellar mass, while stellar age gradients are independent of stellar mass. Li et al. (2018) using MaNGA galaxies with $9 < \log(M_*/\mathrm{M}_\odot) < 12.3$ found metallicity gradients consistent with those of Kuntschner et al. (2010). Moreover, Li et al. (2018) found that stellar metallicity gradients show a strong dependence on stellar velocity dispersion: they peak (being most negative) at velocity dispersions of around 100 km s^{-1}. This radial dependence can be interpreted in terms of different evolutionary scenario for galaxies with different velocity dispersions. In particular, metallicity gradients tend to flatten at high velocity dispersions, perhaps indicating the rising role of mergers that redistribute stellar populations in these galaxies.

However, studies conducted so far that involve IFS surveys are also sometimes in disagreement. For example, Goddard et al. (2017a) selected ETGs from MaNGA with $9 < \log(M_*/\mathrm{M}_\odot) < 11.5$. Although the galaxies were drawn from the same survey as used by Li et al. (2018), the authors derived metallicity profiles that become steeper towards higher masses. A similar result was found by Zheng et al. (2017), for ETGs in the MaNGA survey with $8.5 < \log(M_*/\mathrm{M}_\odot) < 11.5$. In Greene et al. (2015), subsequently extended in Greene et al. (2019) to larger radii, ETGs with $\log(M_*/\mathrm{M}_\odot) > 11.6$ show shallow metallicity gradients and radius-independent age and α-element abundances relative to iron, i.e. [α/Fe]. By analysing a sample of 96 passive brightest cluster galaxies (BCGs) from the SAMI survey, Santucci et al. (2020) found negative metallicity gradients that tend to become shallower as the stellar mass increases, slightly positive age gradients and almost zero [α/Fe] gradients, the latter tending to become slightly more negative with increasing mass. This study also revealed there to be no significant differences in the stellar profiles of the analysed properties between central and satellite galaxies, both at fixed stellar mass and as a function of halo mass, suggesting that the two galaxy populations follow a similar formation scenario, which appears to be independent of the environment. Differences among these various studies (also when using the same galaxy survey) appear to result from a combination of different selection criteria adopted to identify ETGs, the stellar mass ranges considered, and the methods used to retrieve properties and their profiles. In addition, we have found that the radial range adopted to measure the gradients and whether the profiles are stacked in physical units or in units of R_e, can lead to some of these discrepancies.

Despite the relatively large number of IFS surveys, understanding whether a stellar population in a galaxy either formed in situ or was accreted from another progenitor is not a trivial task. Oyarzún et al. (2019), analysing more than 1000 ETGs with $10 < \log(M_*/\mathrm{M}_\odot) < 12$ from the MaNGA survey, studied the radial distributions of metallicity adopting three different stellar fitting codes, i.e. FIREFLY (Wilkinson et al. 2017; Comparat et al. 2017; Goddard et al. 2017b; Maraston & Strömbäck 2011; Maraston et al. 2020), Prospector (Leja et al. 2017; Johnson et al. 2019) and pPXF (Cappellari & Emsellem 2004; Cappellari 2017). As the mass increases, the flattening in the metallicity profiles was found to become more prominent at $R \gtrsim R_\mathrm{e}$. Oyarzún et al. (2019) interpreted this flattening using a toy model in which they assume that the low-mass tail of galaxies in their sample are representative of galaxies mainly constituted by stars formed in situ. For high-mass galaxies, the inner part of the profiles ($R \lesssim R_\mathrm{e}$) is associated with an in-situ stellar population, while the external parts are considered to be dominated by stars accreted from other galaxies. Quantitatively, they infer the contribution of ex-situ stars within $R \approx 2R_\mathrm{e}$ to be $\approx 20\%$ of the total stellar mass in ETGs with $\log(M_*/\mathrm{M}_\odot) < 10.5$, while in ETGs with $\log(M_*/\mathrm{M}_\odot) > 11.5$ this fraction reaches $\approx 80\%$ (consistent results are also presented in the observational works of Edwards et al. 2020 and Davison et al. 2021).

An alternative approach that allows to combine observations and simulations has been recently proposed by Nanni et al. (2022). In that paper, the authors built iMaNGA, a MaNGA-like galaxy sample considering both early- and late-type galaxies extracted from the cosmological simulation TNG50 (Nelson et al. 2019b; Pillepich et al. 2019). Specifically, Nanni et al. (2022), collecting simulated galaxies from the snapshots between $z = 0.01$ and $z = 0.15$, so that covering the whole MaNGA redshift range, took into account all the instrumental effects and methods employed to acquire data for MaNGA sources. The specific use of TNG50 allowed the authors to take all the advantages of high-spatial-resolution data, and generate corresponding mock galaxy spectra. Along similar lines, Bottrell & Hani (2022) presented RealSim-IFS5, a generalised tool for forward-modelling realistic synthetic IFS observations from hydrodynamical simulations. RealSim-IFS is able to reproduce cubes similar to those produced by the MaNGA survey Data Reduction Pipeline. Furthermore, extracting around 900 galaxies with $\log(M_*/\mathrm{M}_\odot) > 10$ from TNG50, Bottrell & Hani (2022) applied RealSim-IFS to generate a synthetic MaNGA stellar kinematic survey.

In this work, we propose a physically-grounded model to provide an interpretative scenario for the radial distributions of stellar properties in observed ETGs in terms of in-situ and ex-situ stellar components. In particular, we compare the radial profiles of stellar mass surface density, metallicity, age and line-of-sight velocity dispersion of observed galaxies drawn from the data release 15 of the MaNGA survey with those of simulated ETGs extracted from the TNG100 simulation of the *The Next Generation* Illustris project (IllustrisTNG[1]; Springel et al. 2018; Nelson et al. 2018; Pillepich et al. 2018b; Naiman et al. 2018; Marinacci et al. 2018). Simulated galaxies are broken down into in-situ and ex-situ stellar populations using the methods presented in Rodriguez-Gomez et al. (2015) which serves as a prediction for the gradients of these two populations in massive ETGs. Indeed, the main scope of this work is to suggest a possible evolutionary scenario of the underlying hierarchical stellar mass assembly history of present-day ETGs. With this goal in mind, we focus the analysis on the study of radial distributions of the above-mentioned stellar properties for both MaNGA and IllustrisTNG galaxies, considering quantities *at face value*, i.e. as those directly derived from the pipelines and stellar fitting codes for MaNGA, and those from the TNG100 simulations.

This paper is organised as follows. In section 2 we describe the galaxy samples and the criteria adopted to select ETGs. The method used to compute radial profiles from simulations is described in section 3. Our results are presented in section 4. In section 5 we discuss the implications of the analysis and compare with previous studied, while section 6 presents our conclusions.

Throughout this paper, we assume a ΛCDM cosmological framework with cosmological parameters derived from Planck Collaboration et al. (2016), i.e. $\Omega_{\Lambda,0} = 0.6911$, $\Omega_{m,0} = 0.3089$, $\Omega_{b,0} = 0.0486$, and $H_0 = 67.74\,\mathrm{km\,s^{-1}Mpc^{-1}}$.

2 OBSERVED AND SIMULATED GALAXY SAMPLES

In this section, we describe the selection criteria and physical properties of the observed (MaNGA) and simulated (TNG100) samples and the methods adopted to compare the two samples.

2.1 The MaNGA survey

The MaNGA survey (Bundy et al. 2015; Yan et al. 2016b), one of the three components of the fourth generation of SDSS (York et al. 2000; Gunn et al. 2006; Blanton et al. 2017) mapped with the 2.5 m telescope Apache Point Observatory ≈ 10000 galaxies with $\log(M_*/\mathrm{M}_\odot) > 9$ in the redshift range $0.01 \lesssim z \lesssim 0.15$, providing spatially-resolved spectra for each source. The galaxy sample is taken from an extended version of the original NASA-Sloan Atlas (NSA `v1_0_1`[2]; Blanton et al. 2011) catalogue. By exploiting the IFS technique (Smee et al. 2013; Drory et al. 2015; Law et al. 2015), galaxies in MaNGA are observed with a set of 17 hexagonal bundles, each composed of fibers with a diameter that varies from 12″ (with 19 fibers) to 32″ (with 127 fibers). Each fiber has a diameter of 2″. MaNGA achieves a uniform radial coverage of galaxies to $1.5\,R_\mathrm{e}$ and $2.5\,R_\mathrm{e}$, for ≈ 2/3 (*Primary Sample*) and ≈ 1/3 (*Secondary Sample*) of the final sample. The observations provide a wavelength coverage in the range 3600−10300 Å, with a spectral resolution of $R \sim 1400$ at $\lambda \sim 4000$ Å and $R \sim 2600$ at $\lambda \sim 9000$ Å (see Smee et al. 2013).

The MaNGA observations used in this work were previously reduced by the Data Reduction Pipeline (DRP; Law et al. 2016; Yan et al. 2016a). Both the de-projected distances and stellar kinematic maps are computed using the Data Analysis Pipeline (DAP; Westfall et al. 2019) for MaNGA. The MaNGA galaxies forming our observed sample are taken from the SDSS data release 15 (DR15, hereafter simply MaNGA; Aguado et al. 2019) which corresponds to the first 4675 observed MaNGA galaxies[3].

To study the behaviour of radial profiles of observed ETGs we use measurements of stellar mass surface density, metallicity, and age derived from two full spectral fitting codes: FIREFLY[4] (Wilkinson et al. 2017; Comparat et al. 2017; Goddard et al. 2017b; Maraston & Strömbäck 2011; Maraston et al. 2020) and Prospector[5] (Leja et al. 2017; Johnson et al. 2019). The use of two different methods will help to quantify the presence of systematic biases caused by different assumptions, priors and fitting methods (Conroy 2013). In addition, we take into account estimates of line-of-sight stellar velocity dispersion obtained by using the pPXF code[6] (Cappellari & Emsellem 2004; Cappellari 2017). In the following we briefly summarise the settings adopted for the three stellar population fitting codes.

- FIREFLY (Fitting IteRativEly For Likelihood analYsis) is a χ^2-minimisation fitting code for deriving the stellar population properties. This code aims at disentangling stars and dust, subtracting the low-order continuum shape before fitting spectra. A set of simple stellar populations (SSPs) with a variety of age and metallicity are considered iteratively, in order to minimise the χ^2 fitting procedure, allowing FIREFLY to fit non-parametric star formation histories (SFHs). We adopt the stellar population models of Maraston & Strömbäck (2011), the MILES stellar library (Sánchez-Blázquez et al. 2006; Vazdekis et al. 2010), and a Chabrier (2003) IMF. The set of SSPs used are spread over the range 6.5 Myr−15 Gyr in age, while metallicity can assume values in the range $-2.3 \leq \log(Z_*/Z_\odot) \leq 0.3$. The wavelength range covered by the library is 4000−7400 Å. We include only spectra with $S/N > 10$

---

[1] Official website at `https://www.tng-project.org`.

[2] Available at `https://www.sdss.org/dr15/manga/manga-target-selection/nsa/`.

[3] Available at `https://www.sdss.org/dr15/manga/manga-data/`.

[4] Available at `https://github.com/FireflySpectra/firefly_release`.

[5] Available at `https://github.com/bd-j/Prospector`.

[6] Available at `http://www-astro.physics.ox.ac.uk/~mxc/software/`

Table 1. List of priors used for our Prospector runs. Column 1: parameter. Column 2: prior.

Parameter	Prior
Star formation history	Continuity
dust2	TopHat $(0, 1)$
Stellar metallicity $\log Z_*$ $[Z_\odot]$	TopHat $(-2, 0.3)$
Formed stellar mass $M_*/\mathrm{M}_\odot$	LogUniform$(10^7, 10^{12})$
Velocity dispersion σ_* $[\mathrm{km\,s^{-1}}]$	TopHat $(0.1, 400)$

(see Wilkinson et al. 2017; Goddard et al. 2017a), and we mask emission lines.

- Prospector is a code able to infer stellar population properties from photometric and/or spectroscopic data with flexible models. It is based on the original stellar population synthesis code FSPS[7] (Conroy et al. 2009; Conroy & Gunn 2010). Prospector provides the posterior distribution of a stellar population parameter space (externally defined by users), uncertainties, and degeneracies. We adopt the MILES stellar population library, the MIST isochrones (Dotter 2016; Choi et al. 2016) and a Kroupa (2001) IMF[8]. The fitting procedure explores a ten-dimensional parameter space. In this fit, the dust optical depth in the V-band, stellar mass, stellar velocity dispersion, and mass-weighted metallicities are taken into account. Moreover, non-parametric SFHs with a continuity prior are considered. Following the same approach described in Leja et al. (2019), our parameter space considers the star formation rate (SFR) spanning the following time intervals: $0 < t < 30$ Myr, $30\,\mathrm{Myr} < t < 100$ Myr, $100\,\mathrm{Myr} < t < 330$ Myr, $330\,\mathrm{Myr} < t < 1.1$ Gyr, $1.1\,\mathrm{Gyr} < t < 3.6$ Gyr, $3.6\,\mathrm{Gyr} < t < 11.7$ Gyr and $11.7\,\mathrm{Gyr} < t < 13.7$ Gyr. The priors used for our Prospector runs are listed in Table 1. Finally, the posterior distributions are obtained exploiting the Dynamic Nested Sampling package `dynesty` (Speagle 2020).
- The Penalized Pixel-Fitting method (pPXF) code derives the stellar or gas kinematics and stellar population from absorption-line spectra of galaxies, using a maximum penalized likelihood method. The original approach was presented in Cappellari & Emsellem (2004) and then improved in Cappellari (2017). We used pPXF to estimate line-of-sight velocity dispersions for our observed ETGs. The penalisation of pixels that are not well fit minimises the mismatch with the templates employed. We ran pPXF with the MILES library.

2.2 TNG100 simulation

In this work, we extract simulated ETGs from IllustrisTNG[9] (Springel et al. 2018; Nelson et al. 2018; Pillepich et al. 2018b; Naiman et al. 2018; Marinacci et al. 2018), the successor to the original Illustris[10] simulation suite (Vogelsberger et al. 2014a,b; Genel et al. 2014; Sijacki et al. 2015). The data are publicly available[11] and presented in Nelson et al. (2019a). IllustrisTNG is a state-of-the art magneto-hydrodynamic cosmological simulation that models the formation and evolution of galaxies within the ΛCDM framework. As its predecessor, IllustrisTNG exploits all the advantages of the *unstructured moving-mesh* hydrodynamic method arepo (Springel 2010), but improves the numerical methods, the subgrid physical model, and the recipe for galaxy feedback both from stars and AGN. In particular, IllustrisTNG is equipped with a novel dual mode (thermal and kinetic) AGN feedback that shapes and regulates the stellar component within massive systems, maintaining a realistic gas fraction (Weinberger et al. 2017). Also the feedback model from galactic winds has been improved to have better representation of low- and intermediate-mass galaxies (Pillepich et al. 2018a).

The IllustrisTNG model was calibrated to significantly reduce tensions between the original Illustris suite and observations. As shown in Figure 4 of Pillepich et al. (2018a), some of these relevant improvements include the star formation rate density as a function of time, the stellar-to-halo mass relation in the present-day Universe, the stellar mass function, the black hole mass−stellar mass relation, the black hole mass−halo mass relation, the gas content within virial radii, and galaxy sizes.

The IllustrisTNG simulation suite consists of three simulation volumes: TNG50 (Nelson et al. 2019b; Pillepich et al. 2019), TNG100 and TNG300, corresponding to three different box sizes with sides of about 50 Mpc, 100 Mpc and 300 Mpc, respectively. The project assumes a ΛCDM cosmology with cosmological parameters taken from Planck Collaboration et al. (2016). Each run starts at $z = 127$ using the Zeldovich approximation and evolves down to $z = 0$.

We use the highest-resolution version of the medium volume size TNG100, i.e. TNG100-1 (hereafter, simply TNG100). This run includes approximately 2×1820^3 resolution elements. The dark matter (DM) and baryonic mass resolutions are $m_{\mathrm{DM}} = 7.5 \times 10^6\,\mathrm{M}_\odot$ and $m_{\mathrm{b}} = 1.4 \times 10^6\,\mathrm{M}_\odot$. The softening length employed for this version for both the DM and stellar components is $\epsilon = 0.74$ kpc, while an adaptive gas gravitational softening is used, with a minimum $\epsilon_{\mathrm{gas,min}} = 0.185$ kpc. In particular, we take into account the properties of subhalos from snapshot #91, corresponding to $z = 0.1$, close to the mean redshift of galaxies in the MaNGA survey.

2.2.1 In-situ & ex-situ stars in IllustrisTNG galaxies

In the last decade, cosmological simulations have suggested that accretion contributes to the mass and size growth of massive galaxies. The fraction of accreted stars depends on the stellar and DM masses (e.g., Oser et al. 2010; Lackner et al. 2012; Pillepich et al. 2014). From the original Illustris simulation suite, Rodriguez-Gomez et al. (2016) derived the ex-situ fraction for galaxies with stellar masses between $10^9\,\mathrm{M}_\odot$ and $10^{12}\,\mathrm{M}_\odot$. They found that this fraction increases from $\lesssim 10\%$ in the least massive galaxies to above 80% in the most massive systems. A similar analysis has been conducted on the IllustrisTNG runs: Pillepich et al. (2018b) analysed stellar masses within different apertures and found that, at $z = 0$, the low-mass tail of galaxies are mainly formed by in-situ stellar particles, while central galaxies living in the most massive halos, i.e. $\log(M_{200\mathrm{c}}/\mathrm{M}_\odot) > 14$, accreted more than 80% of their total stellar mass via mergers. Moreover, by considering stellar masses within an aperture larger than 100 kpc, the ex-situ fraction is found to be dramatically dominant at these distances, exceeding sometimes 90% of the total mass. The relative contribution in massive systems of the ex-situ component reaches around 60% in the innermost regions (< 10 kpc).

In this paper, we adopt the same definition of in-situ and ex-

---

[7] Available at `https://github.com/cconroy20/fsps`.

[8] For our purpose, the assumption of a Kroupa IMF or a Chabrier IMF to retrieve stellar population properties is almost indistinguishable.

[9] Official website at `https://www.tng-project.org`.

[10] Official website at `https://www.illustris-project.org`.

[11] https: //www.illustris-project.org/data/

situ stars as used in Rodriguez-Gomez et al. (2016), Pillepich et al. (2018b), and Tacchella et al. (2019), exploiting the method for reconstructing the baryonic merger trees of Rodriguez-Gomez et al. (2015):

- *in-situ stars* are those stellar particles that formed in a galaxy belonging to the main progenitor branch of the merger tree.
- *ex-situ stars* are those stellar particles that, at the time of their formation, were bound to a galaxy outside the main progenitor branch of the descendant galaxy.

2.3 ETG selection

We aim to perform a comparison that is as consistent as possible between TNG100 and MaNGA. The first question at hand is how to select ETGs. We opt for a simple selection based on $(g-r)$ rest-frame colours, identifying hereafter ETGs as *Red Galaxies*, that is those galaxies with $(g-r) > 0.6$, a value that marks the transition between the blue cloud and the red sequence of galaxies. Nelson et al. (2018) consider three models for assigning *ugriz* magnitudes to simulated galaxies, comparing them with those of SDSS galaxies. The authors discuss in detail the results obtained using colours derived through the so-called *resolved dust model* (Model C) which accounts for the presence of dust, following the distribution of neutral gas in galaxies, and adding also the attenuation caused by the presence of metals. The data from Model C are available in the supplementary catalogue SDSS Photometry, colours, and Mock Fiber Spectra[12]. In Nelson et al. (2018), the IllustrisTNG colours were compared with the observed colours of SDSS DR12 (Alam et al. 2015) galaxies in the present-day Universe ($z < 0.1$). The distributions of $(g-r)$ colours recovers the colour bimodality of SDSS galaxies. In SDSS, the blue and red simulated galaxy populations show two characteristic peaks at $(g-r) \approx 0.4$ and ≈ 0.8, respectively. Moreover, above $M_* \simeq 10^{10.5}\,\mathrm{M}_\odot$ the colour bimodality tends to disappear and red galaxies dominate. For this paper, to select ETGs in our observed MaNGA sample, we retrieved the *ugriz* Petrosian magnitudes from the NSA catalogue. To sum up, in the following, we will present the results of our analysis for MaNGA and TNG100 ETGs selected as such considering only objects with $(g-r) > 0.6$.

2.4 Stellar mass estimates

Another question to consider when comparing observations and simulations is the consistency of the stellar mass measurements. Indeed, differences in the measurements of stellar masses can be caused by several factors, such as the fitting method used to derive luminosities and colours, as well as the stellar population synthesis models and libraries assumed. Sonnenfeld et al. (2019) discuss the differences in deriving luminosity of galaxies in massive ETGs observed with the Hyper-Supreme Cam (HSC; Miyazaki et al. 2018) Subaru Strategic Program (Aihara et al. 2018, DR1), assuming either a simple Sérsic fit or a Sérsic+Exponential fit. The difference between the two methods can cause a variation of around 0.1 dex on the measurements of luminosity for the same object. Moreover, a different assumption of IMF can imply a global shift of stellar masses and the potential presence of IMF radial variations can introduce biases. The radius used to estimate stellar mass, or the quality of the observational data, can also be an important factor (e.g., Huang et al. 2018; Ardila et al. 2021).

In this work we assume the stellar mass estimates from the UPenn_PhotDec_MsSTAR[13] catalogue of Meert et al. (2015) for MaNGA ETGs. In particular, these stellar masses, obtained by multiplying the stellar mass-to-light ratios (M_*/L) from Mendel et al. (2014) by the luminosities from the PyMorph SerExp (Sérsic+Exponential) photometry, assume M_*/L fitting models that account for the effects of dust extinction (Table 3 of Mendel et al. 2014).

For TNG100 galaxies we consider the 2D projected stellar mass defined as the sum of all bound stellar particles within a projected radius $R = 2R_{\mathrm{hm}}$, where R_{hm} is the radius of a circle containing half of all stellar particles bound to each subhalo. Hereafter, we will refer to *2hmr mass* as the projected mass within a radius of $R = 2R_{\mathrm{hm}}$.

Table 2 summarises the properties of the final TNG100 and MaNGA *Red Galaxy samples*, i.e. objects with $\log(M_*/\mathrm{M}_\odot) \geq 10.5$ and $(g-r) > 0.6$. Figure 1 shows the colour–mass diagrams and the stellar mass distributions of both samples. As clearly visible, the distribution of the stellar masses for MaNGA galaxies appears almost flat. The reason for such distribution is due to the original MaNGA sample design: as argued in Wake et al. (2017), the MaNGA sample was built in such a way that the most massive galaxies are located at higher redshifts, but, at the same time, both the Primary and Secondary samples are selected to have flat stellar mass distributions. We will account for this effect later in the paper.

3 RADIAL PROFILES OF STELLAR PROPERTIES

In subsection 3.1 and subsection 3.2 we describe the method used to compute the radial profiles from the observed and simulated 2D stellar galaxy images. In subsection 3.3 and subsection 3.4 we describe how we compute median profiles in different stellar mass bins.

3.1 Radial profiles for MaNGA ETGs

To obtain stellar properties at different galactocentric distances for each MaNGA galaxy we adopt the approach described in Oyarzún et al. (2019), with the difference that we consider radial binning in physical units instead of units of effective radii. Specifically, by considering the axis ratio of each source obtained from r-band photometric images, elliptical polar radii are associated to spaxels. We then bin in five concentric elliptical annuli each galaxy map, assuming the following radii as the edges of each bin: $R/\mathrm{kpc} = \{0;\ 2;\ 4;\ 10;\ 20;\ 100\}$. The choice of using a radial binning in physical units is justified by the fact that effective radius measurements may be affected by the depth of the survey. For example, HSC measures different effective radii than SDSS (Huang et al. 2018).

The next step after radial binning consists in shifting spectra to the rest-frame by taking the stellar systemic velocity from DAP as a reference. A Voronoi binning is then applied to the maps, considering a minimum $S/N = 10$ in each bin. Spectra belonging to the same annulus are co-added and, after running pPXF with the

---

[12] Available at `https://www.tng-project.org/data/downloads/TNG100-1/`.

[13] Available at `http://alan-meert-website-aws.s3-website-us-east-1.amazonaws.com/fit_catalog/download/index.html`.

Table 2. Summary table of the MaNGA and TNG100 samples. Column 1: sample. Column 2: number of ETGs. Column 3: stellar mass range. Column 4: mean stellar mass. Column 5: median stellar mass. Stellar masses are in units of $M_\odot$.

Sample	$N_{\rm ETG}$	$(\log M_{*,\rm min}; \log M_{*,\rm max})$	$\log M_{*,\rm mean}$	$\log M_{*,\rm median}$
MaNGA	1427	(10.50; 12.26)	11.07	11.04
TNG100	1543	(10.50; 12.27)	10.83	10.76

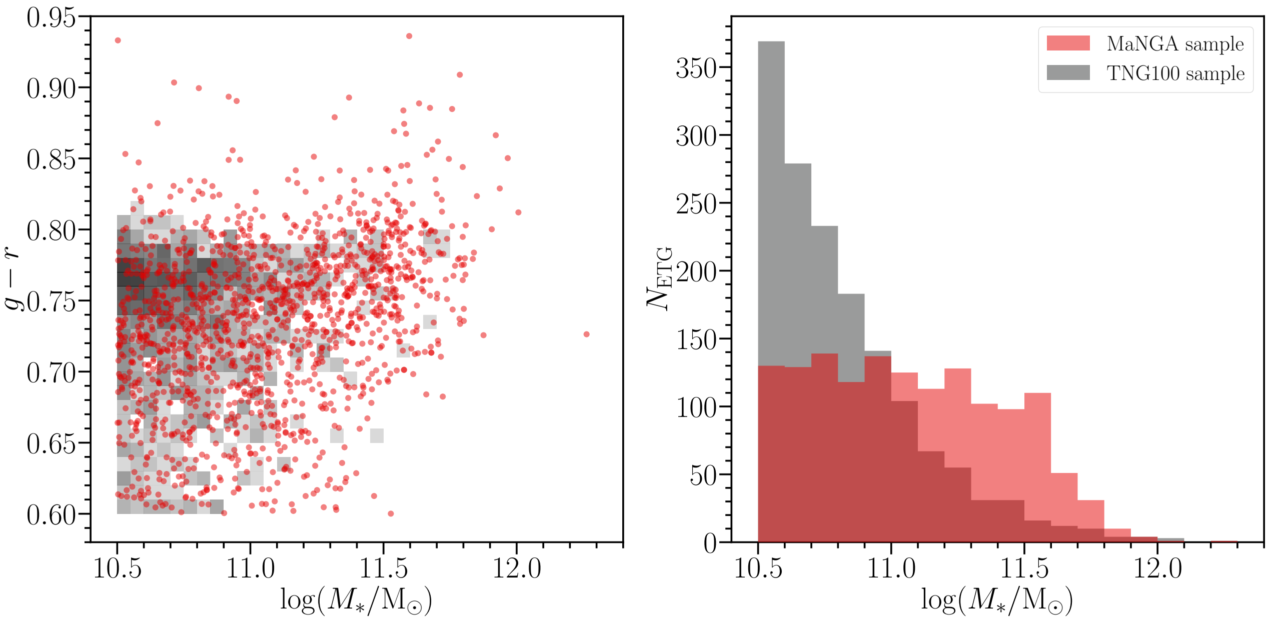

Figure 1. Left: MaNGA (red dots) and TNG100 (2D grey histogram) ETGs. Right panel: 1D histograms of the mass distribution for the MaNGA (red histogram) and the TNG100 (grey histogram) estimates. The histogram of MaNGA ETGs stellar masses is flat due to the MaNGA selection function (see Wake et al. 2017).

MILES library, they are stacked to estimate the line-of-sight stellar mean velocity and velocity dispersion.

3.2 Radial profiles for TNG100 ETGs

To obtain the radial profiles of stellar properties for TNG100 galaxies, we apply the same method presented in Ardila et al. (2021). We firstly project the 3D particle distributions of simulated galaxies on a 2D $X-Y$ plane using the `hydrotools` package (Diemer et al. 2018, 2019). For each subhalo, the 2D map consists of 300 pixels per side, with a resolution of 1 kpc per pixel (for a total physical side length of the map of 300 kpc). To extract the 1D stellar profiles we then use the method presented in Huang et al. (2018) and also used by Ardila et al. (2021), which we now briefly describe. We extract 1D stellar mass surface density profiles using the galaxy surface brightness profile function included in the `kungpao` package[14]. Galaxy centroids are identified by means of `extract`, a function included in the `sep` library, and the `ellipse` algorithm is used to fit concentric elliptical isophotes. The position angle and ellipticity of these isophotes are the mean values from the 2D fitting procedure of the galaxy maps. The isophotes are spread over the range 1−150 kpc, in 20 concentric elliptical annuli of constant width in logarithmic space. For stellar metallicity, age, and line-of-sight velocity dispersion profiles, we use the same centre and ellipticity of the isophotes computed on the stellar mass surface density mass maps. To derive mass-weighted stellar metallicity, age, and velocity dispersion each pixel is weighted by the corresponding value of stellar mass in that pixel. The entire procedure is applied to both the in-situ and ex-situ stellar populations, starting from their 2D stellar property maps.

Another effect we accounted for is about the differences in spatial resolutions. For this, we associate each simulated galaxy an angular diameter distance, assuming a redshift drawn from the $z-M_*$ distribution of the MaNGA sample (see Figure A1 in Appendix A). For each TNG100 ETG, we smooth the galaxy map with a 2D Gaussian filter kernel:

$$\sigma_{{\rm kernel},i} = \sqrt{\mathcal{R}^2_{{\rm MaNGA},i} - \mathcal{R}^2_{\rm TNG}}, \tag{1}$$

where $\mathcal{R}_{\rm TNG} = 1\,{\rm kpc}$ is the resolution of the TNG100 sample, $\mathcal{R}_{{\rm MaNGA},i} = \sin({\rm PSF}_{\rm MaNGA}) d_{A,i}$, with ${\rm PSF}_{\rm MaNGA} = 2.5''$ ($\simeq 1.21 \times 10^{-5}$ in radians), and $d_{A,i}$ is angular diameter distance (in kpc) for the i-th galaxy in the TNG100 sample determined as described above. For example, at $z = 0.05$, $\mathcal{R}_{\rm MaNGA} \simeq 2.52\,{\rm kpc}$. For a given simulated ETG we compute two types of radial profiles for each stellar physical property (for both the in-situ and ex-situ

---

[14] The `kungpao` library is available at `https://github.com/dr-guangtou/kungpao/`

Table 3. Hyper-parameters used to compute MaNGA and TNG100 profiles of stellar properties. Column 1: stellar property. Column 2: uniform prior on the mean (lower bound; upper bound). Column 3: uniform prior on the intrinsic scatter (lower bound; upper bound).

Stellar property	$(\mu_{\rm min}; \mu_{\rm max})$	$(\sigma_{\rm min}; \sigma_{\rm max})$
Surface density $\log \Sigma_*$ [$\mathrm{M_\odot\,kpc^{-2}}$]	(0; 11)	(0; 2)
Metallicity $\log Z_*$ [$\mathrm{Z_\odot}$]	(−1; 1)	(0; 1)
Age [Gyr]	(0; 13)	(0; 5)
Velocity dispersion σ_* [$\mathrm{km\,s^{-1}}$]	(0; 350)	(0; 100)

stellar populations): the *uncovolved profile* and the *convolved profile*, the latter obtained by smoothing the projected maps with the 2D Gaussian filter kernel $\sigma_{\rm kernel}$.

3.3 Building stellar mass bins

To compare the profiles of stellar properties between MaNGA and TNG100, we divide galaxies into bins of stellar mass and compute the median profile in each stellar mass bin along with the associated uncertainties. As a fiducial choice, we compare galaxies at *fixed stellar mass*. The three stellar mass bins used are $10.5 \leq \log(M_*/\mathrm{M_\odot}) < 11$, $11 \leq \log(M_*/\mathrm{M_\odot}) < 11.5$, and $\log(M_*/\mathrm{M_\odot}) \geq 11.5$. In Appendix B, we present the same analysis using number-density-based bins, highlighting the differences with respect to the use of bins at fixed stellar mass.

3.4 Building median radial profiles with errors

We use a Bayesian hierarchical approach (e.g., Cannarozzo et al. 2020) to estimate the median values and the associated 1σ uncertainties on the observed and simulated radial profiles. We assume that each stellar property X in any radial bin has a Gaussian distribution, so that its likelihood can be written as

$$\mathrm{P}(X|X^{\rm data}, \sigma_X^{\rm data}, \mu, \sigma) = \frac{1}{\sqrt{2\pi\sigma_X^2}} \exp\left\{-\frac{(X^{\rm data}-\mu)^2}{2\sigma_X^2}\right\}, \qquad (2)$$

where X is the quantity that we want to infer in each radial bin (e.g., the logarithm of the stellar mass surface density), while $X^{\rm data}$ and $\sigma_X^{\rm data}$ are the data values and their related uncertainties, respectively. The variance in Equation 2 has the form

$$\sigma_X^2 = {\sigma_X^{\rm data}}^2 + \sigma^2. \qquad (3)$$

In Equation 2 and in Equation 3, μ and σ are the two *hyper-parameters* of our Bayesian hierarchical approach and represent the mean value and the intrinsic scatter of the distribution of the quantity X, respectively. We underline that, in the case of simulated ETGs, Equation 3 reduces to $\sigma_X^2 = \sigma^2$, since no uncertainties are associated to simulated properties. These parameters are estimated independently in each bin. In Table 3, we list the priors adopted for each property. The stellar properties of MaNGA and TNG100 galaxies are sampled adopting a Markov chain Monte Carlo (MCMC) approach using 10 random walkers and 300 steps (removing the first 200 steps) for each run to reach the convergence of the hyper-parameter distributions. We use the Python adaptation of the affine-invariant ensemble sampler of Goodman & Weare (2010), EMCEE by Foreman-Mackey et al. (2013).

3.5 MaNGA and TNG100 stellar properties

In our comparison between MaNGA and TNG100 ETGs, we consider the circularised radial distributions of the stellar mass surface density Σ_*, stellar metallicity Z_*, stellar age, and line-of-sight stellar velocity dispersion σ_*.

As already described in subsection 3.1 and in subsection 3.2, in order to construct the radial profiles of the aforementioned properties, we build 5 concentric radial bins for MaNGA ETGs from the innermost regions out to 100 kpc and 20 log-spaced bins out to 150 kpc for TNG100 objects, for which we are able to split the relative contribution of in-situ and ex-situ stellar populations. We make use of mass-weighted stellar metallicities and ages for both MaNGA and TNG100 galaxies. For these two properties, we also tested the luminosity-weighted measurements for MaNGA galaxies finding no significant difference between the two choices. Velocity dispersions, instead, are mass weighted for simulated galaxies and luminosity-weighted for observed sources [15].

The stellar mass surface density, metallicity and age measurements for MaNGA sources are computed using both FIREFLY and PROSPECTOR, while for line-of-sight velocity dispersions we use PPXF (see subsection 2.1). For MaNGA galaxies, the median profiles and related uncertainties in each radial bin are computed as described in subsection 3.4, but imposing the condition that the measurements are available for at least 75% of the sample in each stellar mass bin. FIREFLY and PROSPECTOR measurements are derived using stellar population libraries that assume different values of solar metallicity ($\mathrm{Z_{\odot,FIREFLY}} = 0.019$ and $\mathrm{Z_{\odot,P{\scriptsize ROSPECTOR}}} = 0.0142$). For this reason, to homogenise and make comparisons easier, all the observed and simulated stellar metallicity profiles are normalised by their respective values at ≈ 7 kpc, which corresponds to the median radius of the the third MaNGA bin.

Since our main goal is to provide a possible evolutionary scenario on how present-day Universe ETGs have been formed throughout the cosmic history, all the stellar properties considered in this work (for both observed and simulated objects) are *at face value*, i.e. as directly derived from pipelines and fitting codes for MaNGA, and from output catalogues for TNG100. Thus, no mock observational data of simulated galaxies have been produced, as instead done for instance by Nanni et al. (2022).

4 RESULTS

We now compare the stellar mass surface density, metallicity, age, and line-of-sight velocity dispersion profiles obtained for our observed and simulated samples of ETGs. We focus here on the results corresponding to the stellar mass bins. The results for the number-density-based bins are shown in Appendix B.

---

[15] For TNG100 galaxies, the maps of stellar metallicity, age, and velocity dispersion are all weighted by stellar masses for consistency within the simulated sample. We note that, for the velocity dispersion, the comparison between simulated and observed galaxies is not fully self-consistent, because the velocity dispersion of the MaNGA galaxies is weighted by luminosity. However, as shown in Figure 2, the simulated galaxies have old stellar populations ($\gtrsim 7$ Gyr), responsible for their red colours. Moreover, the age distributions of TNG100 galaxies are almost flat at all stellar masses, in particular going towards the high-mass tail, suggesting the presence of similar stellar populations. In light of that, we do not expect for our sample of old and red galaxies (selected as such as described in subsection 2.3) a significant discrepancy between mass- and luminosity-weighted velocity dispersion profiles.

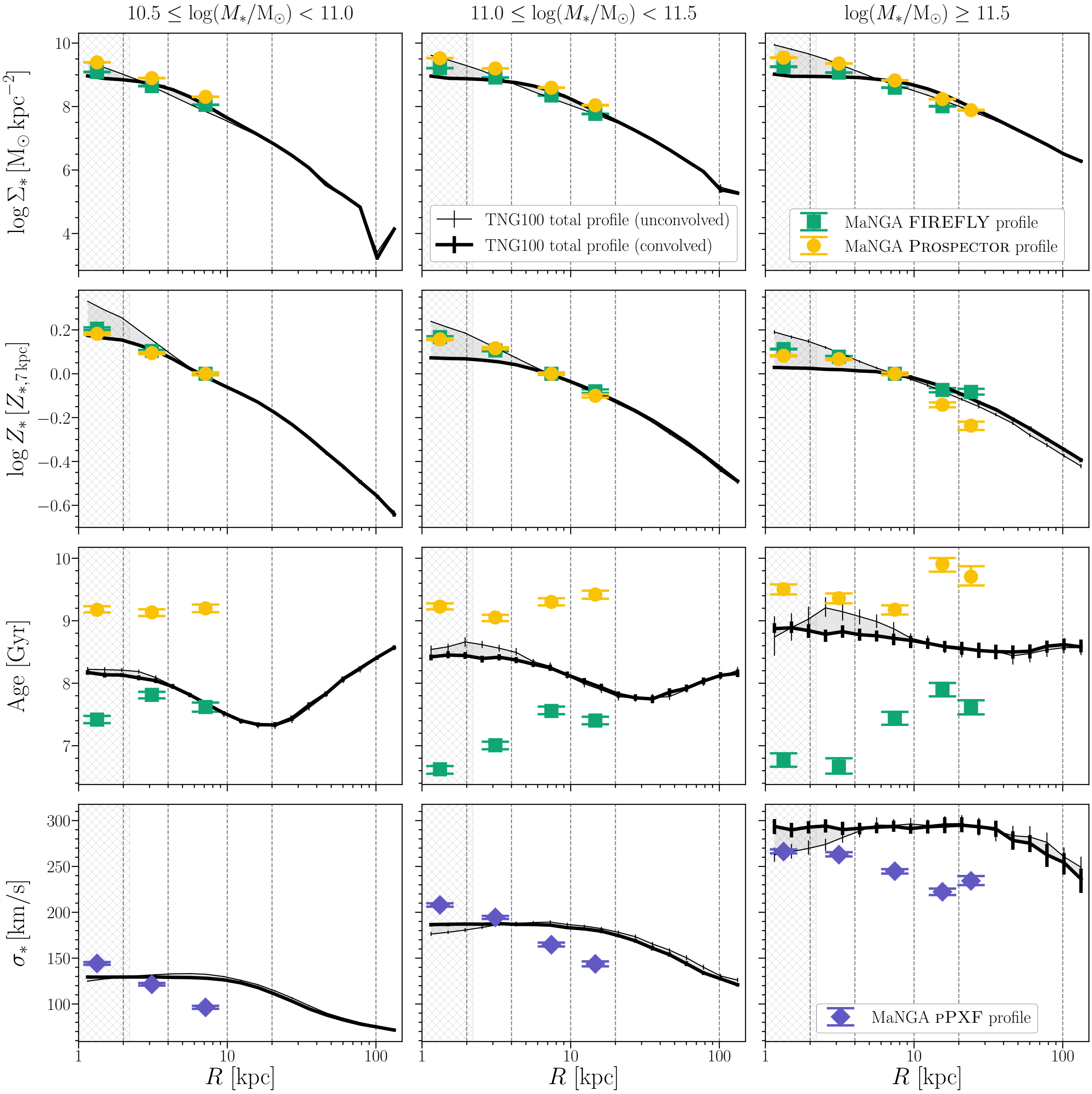

Figure 2. Radial profiles of stellar mass surface density, metallicity (normalised by the corresponding values of metallicity at ≈ 7 kpc), age, and line-of-sight velocity dispersion (from top to the bottom) in three bins of stellar mass for MaNGA and TNG100 ETGs. Green, yellow and violet dots represent the median estimates respectively for MaNGA galaxies from FIREFLY, Prospector and pPXF. Both the stellar metallicity and age measurements in MaNGA and TNG100 ETGs are mass weighted. Velocity dispersions are luminosity weighted for MaNGA and mass weighted for TNG100 sources. The vertical grey dashed lines indicate the 5 radial bins for MaNGA. The two black curves represent the median values of each stellar property for the total stellar population in TNG100. The intrinsic profiles are shown with the thin curve whereas the thick curves indicate the results when convolved with the MaNGA PSF. The light grey hatched area ($R \lesssim 2.1$ kpc) shows three times the gravitational softening length of the stellar particles in TNG100. The grey shaded area is the region that lies in between the profiles obtained from the original and the convolved TNG100 maps. Because we account for the MaNGA PSF but not for the effects of the resolution of the simulation, the grey shaded area gives a sense of the uncertainty in the comparison in the inner regions. The errorbars represent the 1σ uncertainties on the median for MaNGA and TNG100 estimates.

4.1 Stellar mass surface density profiles

Figure 2 shows the results for the total stellar populations. For TNG100, both the raw profiles and profiles convolved with the MaNGA PSF are displayed. We show profiles both using the median estimates from FIREFLY (yellow dots) and Prospector (green squares). In each stellar mass bin, we find a satisfying agreement at all radii between the two MaNGA measurements, with a small systematic shift to higher values with Prospector. This is consistent with the observed systematic shift in the total mass estimates (for the same galaxy, Prospector infers a stellar mass that, on average, is higher than the estimate obtained by FIREFLY by ≈ 0.15−0.2 dex). In each stellar mass bin, we find a remarkable agreement between

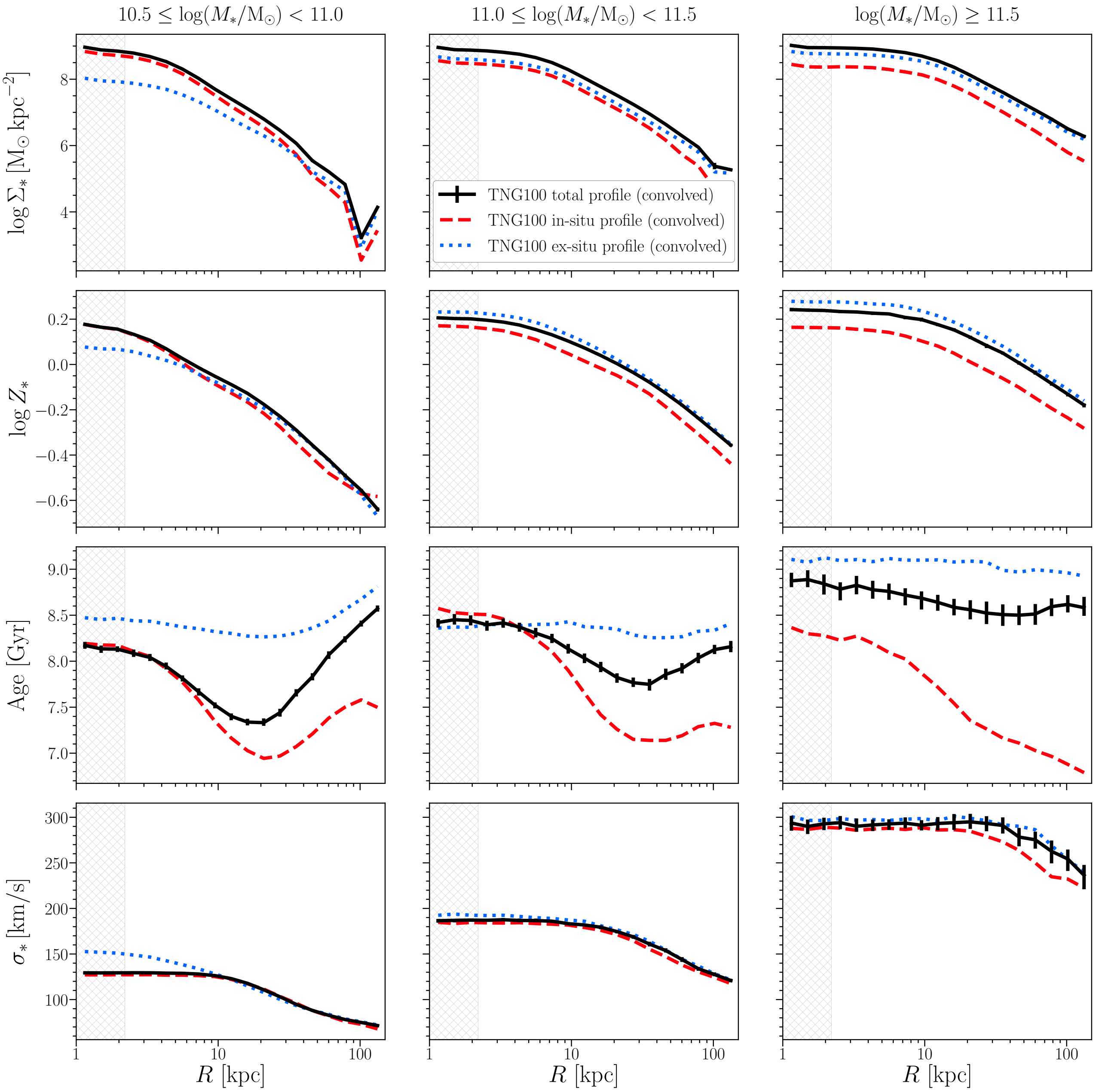

Figure 3. Contribution from in-situ and ex-situ stellar populations to the radial profiles of TNG100 ETGs. Top to bottom corresponds to profiles of stellar mass surface density, metallicity (not normalised), age, and line-of-sight velocity dispersion. The stellar metallicity, age, and velocity dispersion measurements are mass weighted. The black solid, red dashed, and blue dotted curves correspond to the total, in-situ, and ex-situ stellar populations, respectively. For clarity reasons, here we only show the median profiles convolved with the MaNGA PSF, and we omit the errorbars for the in-situ and ex-situ stellar population profiles. The light grey hatched area ($R \lesssim 2.1$ kpc) shows three times the gravitational softening length of the stellar particles in TNG100. *Note*: the range shown along the y-axes are different from those of Figure 2.

the stellar mass surface densities of MaNGA ETGs and those from TNG100, both in the shape and normalisation of the profiles.

In Figure 3 we separate the TNG100 profiles into in-situ (red dashed curves) and ex-situ (blue dotted curves) components. In the mass range $10.5 < \log(M_*/\mathrm{M}_\odot) < 11$, on average, the in-situ stellar component is found to be dominant out to ≈ 30 kpc and ex-situ stars dominate at larger radii. The central mass bin, i.e. $11 < \log(M_*/\mathrm{M}_\odot) < 11.5$, reveals the increasing contribution from ex-situ stars – the profiles of the two populations contribute in almost equal proportions over the entire radial range. Above $\log(M_*/\mathrm{M}_\odot) \approx 11.5$, the ex-situ stars dominate at all radii. To summarise, we find that below $\log(M_*/\mathrm{M}_\odot) \approx 11$ the most relevant stellar component (out to ≈ 30 kpc) is the in-situ population, whereas at higher stellar masses the ex-situ stars become dominant across the entire radial range.

4.2 Metallicity profiles

The second row of plots in Figure 2 displays the metallicity profiles in three stellar mass bins. The two MaNGA profiles show similar radial distributions, which differ only beyond 10 kpc for the most massive systems by a factor $\lesssim 0.2$ dex at ≈ 20 kpc[16].

Globally, TNG100 profiles reproduce fairly well the shapes of the two MaNGA estimates. In particular, below 10^{11} $\mathrm{M}_\odot$, the TNG100 MaNGA-PSF convolved profile reproduces well the median profiles from FIREFLY and Prospector. Over the interval between 10^{11} $\mathrm{M}_\odot$ and $10^{11.5}$ $\mathrm{M}_\odot$, the median profiles of MaNGA ETGs lie in between the two TNG100 profiles derived from the MaNGA-PSF unconvolved and convolved maps within around 4 kpc, and almost overlap beyond this distance with the two TNG100 profiles. Above $10^{11.5}$ $\mathrm{M}_\odot$, the FIREFLY profile is quite well represented even in the outermost regions, while the Prospector distribution tends to assume lower values in metallicity, differing from the TNG100 profiles by a factor of $\lesssim 0.1$ dex. We stress here the importance of applying a smoothing using the MaNGA PSF on the original maps of simulated objects. Indeed, at all bins the stellar metallicity profiles from the original maps are steeper than those obtained from the convolved maps, the latter giving values lower by ≈ 0.15–0.2 dex in the innermost regions ($R \lesssim 4$ kpc).

The necessity of renormalising metallicity measurements to reconcile observations and simulations has been already highlighted by Nelson et al. (2018). The right panel of Figure 2 of Nelson et al. (2018) shows the stellar mass-metallicity relations for TNG100 (and TNG300) compared with observed estimates in the present-day Universe from Gallazzi et al. (2005); Woo et al. (2008); Kirby et al. (2013). Above $\log(M_*/\mathrm{M}_\odot) > 10.5$, simulations and observations almost agree in shape, showing a weak scaling with stellar mass (with a supersolar metallicity normalisation). However, the almost-flat trend of the metallicity as a function of stellar mass in simulations implies a discrepancy of up to ≈ 0.5 dex at $\log(M_*/\mathrm{M}_\odot) < 10.5$ from observed estimates. A possible reason for the origin of such a discrepancy can be found in different methods to derive simulated and observed metallicities. Indeed, when opportune corrections and spectral fitting codes similar to those adopted on observational data are applied to simulated galaxies, the aforementioned discrepancy reduces, making the estimates of TNG100 more consistent with those from observations.

The in-situ and ex-situ PSF-convolved stellar metallicity profiles (second row of plots in Figure 3) are shown without adopting any normalisation. TNG100 galaxies are characterised by ex-situ stars that are more metal rich than the in-situ population: this metallicity difference increases for increasing stellar mass. This apparently counter-intuitive finding could be in tension with the expected scenario from downsizing. A possible explanation for the presence of such metal-rich ex-situ stellar populations in these massive systems could be ascribed to the fact that, because of the substantial ex-situ fraction accreted via major mergers (see section 5) across their stellar mass assembly histories, many galaxies that were centrals at a given snapshot became satellites of lightly more massive systems soon thereafter.

4.3 Age profiles

Figure 2 also displays a comparison between the radial distributions of stellar ages. The stellar age profiles derived from FIREFLY and Prospector show a common behaviour in all mass bins: namely, a systematic shift in age is found between the two stellar fitting codes. On average, FIREFLY and Prospector differ in their age estimates by about 1.5–2.5 Gyr (on average, FIREFLY estimates are $\approx 20\%$ younger than those from Prospector). The systematic difference in age obtained by the two codes might be partially explained in terms of the *age-metallicity degeneracy*: the red colours that characterise old stellar populations can be explained also assuming a higher metallicity, and viceversa (Worthey 1994). Indeed, for the same sample of ETGs, on average, FIREFLY derives more metal-rich and younger stellar populations compared to Prospector. However, this degeneracy should ideally be reflected in the uncertainty values produced by the stellar population synthesis codes. The fact that the measurements are inconsistent may also suggest that elements of the models used by the two codes, such as the stellar libraries, are themselves inconsistent, and not sufficiently flexible. A crucial point is that deriving stellar ages for such old systems is not trivial (see Conroy 2013). Indeed, stellar age grids for these models are sparse at these ages because they tend to be log-spaced. When building non-parametric SFHs, these codes interpolate over the ages sampled by the stellar libraries and isochrones. The large gap between the two stellar age profiles displayed in Figure 2 can be taken as a measure of the systematic uncertainty on the age of the observed galaxies in our sample. It is clear that these age profiles have little constraining power on theoretical models: the TNG100 profiles lie in between FIREFLY and Prospector, reproducing only the quasi-flat distributions of observed data. The analysis of the radial distributions of age for the in-situ and ex-situ stellar populations in the simulated ETGs (see Figure 3) shows that, below $\log(M_*/\mathrm{M}_\odot) \approx 11$, the ex-situ component is older (up to +1.5 Gyr) than the in-situ component over the entire radial range, whereas the inner regions ($R \lesssim 6$ kpc) of galaxies with $11 \lesssim \log(M_*/\mathrm{M}_\odot) \lesssim 11.5$ are composed of in-situ and ex-situ stars with similar ages. Above $\log(M_*/\mathrm{M}_\odot) \approx 11.5$, ex-situ stars are found to be older (up to +2.5 Gyr) than the in-situ population at all radii.

4.4 Velocity dispersion profiles

The bottom panels in Figure 2 compares the radial profiles of line-of-sight stellar velocity dispersions for simulated and observed ETGs. Here, the MaNGA values are derived using the pPXF code. Below $\log(M_*/\mathrm{M}_\odot) \approx 11.5$, we generally find a good first-order agreement in normalisation between MaNGA and TNG100, but the MaNGA profiles are steeper than those of TNG100. More quantitatively, the difference between the two median profiles can be at most of around 30 km s^{-1}. Instead, above $\log(M_*/\mathrm{M}_\odot) \approx 11.5$, the velocity dispersion profiles of both MaNGA and TNG100 galaxies are almost flat out to $R \approx 40$ kpc. However, we find an essentially radius-independent difference between the two profiles, with velocity dispersions for the simulated ETGs generally higher by 30–40 km s^{-1} (this will be discussed further in subsection 4.5). We underline that the effect on the observed velocity dispersion σ_* for MaNGA galaxies is the result of two main contributions, i.e. the instrumental dispersion σ_{inst} and the intrinsic stellar velocity dispersion $\sigma_{*,\mathrm{int}}$:

$$\sigma_*^2 = \sigma_{\mathrm{inst}}^2 + \sigma_{*,\mathrm{int}}^2. \tag{4}$$

In fact, over the rest-frame optical range $0.36 \lesssim \lambda/\mu\mathrm{m} \lesssim 1.03$, the spectral resolution is $R \sim 2000$ and the 1σ dispersion of the instrumental spectral line-spread function is about 70 km/s (see Westfall et al. 2019; Law et al. 2021). As reported in Westfall et al. (2019), for $\sigma_* \gtrsim 100$ km/s, the uncertainties on velocities can be approximated as $\delta(\Delta v) \approx \langle\sigma_*\rangle/(S/N)_g$, where $\langle\sigma_*\rangle$ is the

---

[16] If the two MaNGA stellar metallicity distributions are not renormalised at their ~ 7 kpc values, the FIREFLY profiles, on average, are shifted up from the Prospector profiles by a factor of $\lesssim 0.05$ dex at $\log(M_*/\mathrm{M}_\odot) \lesssim 11.5$, and can differ even of $\lesssim 0.16$ dex for galaxies with $\log(M_*/\mathrm{M}_\odot) \gtrsim 11.5$.

mean velocity dispersion and $(S/N)_g$ is the g-band signal-to-noise ratio. At $(S/N)_g = 10$, the typical uncertainties on velocities are around 10% of σ_*. For $\sigma_* \gtrsim 100\,\mathrm{km/s}$, the uncertainties on velocity dispersions are slightly larger the those of velocities, but can be roughly approximated by a single proportionality constant. Given that, our estimates of velocity dispersion profiles are quite robust, because, on average, these measurements are greater than 100 km/s, with the only exception of the last radial bin of the profile for galaxies with $10.5 \leq \log(M_*/\mathrm{M}_\odot) < 11$, that is around 90 km/s.

The line-of-sight stellar velocity dispersion profiles for the in-situ and ex-situ components (bottom panels in Figure 3) almost coincide in the intermediate and high-mass bins, while in the low-mass bin the velocity dispersion is higher in the centre for the in-situ component. As it is well known, in the same gravitational potential, the line-of-sight stellar velocity dispersion profile of a given component depends on both its intrinsic velocity distribution and its density distribution: in particular, for given velocity distribution, the steeper the density profile, the lower the velocity dispersion (see Nipoti et al. 2021). In the low-mass bin, the higher central velocity dispersion of the in-situ component can be qualitatively explained by its shallower surface density profile (see top-left panel in Figure 3).

4.5 Central versus satellite galaxies

We now consider the radial profiles separately for central and satellite galaxies. Halos and subhalos in IllustrisTNG are detected by SUBFIND, the subhalo finder code developed by Springel et al. (2001). Specifically, an IllustrisTNG subhalo is classified as *central* (flag `is_primary==1`) if it is the subhalo with the deepest potential well among those belonging to the same friends-of-friends (FoF) halo. Otherwise, subhalos are classified as *satellites*. To separate MaNGA ETGs into centrals and satellites we rely on the classification provided by Yang et al. (2007), obtained for a sample of more than 300000 galaxies from SDSS DR4 (Adelman-McCarthy et al. 2006).

Though they are not shown here, we do find that the MaNGA and TNG100 stellar mass surface density profiles, as well as those for the stellar metallicity and age, are in excellent agreement between central and satellite ETGs. This lack of differences in the radial profiles between these two populations is consistent with previous outcomes in literature, as for instance shown by Santucci et al. (2020) for stellar age and metallicity properties.

Centrals and satellites display similar trends also for the in-situ and ex-situ components over the entire mass range considered. We might expect central galaxies to exhibit larger ex-situ components compared to satellites. However, a possible explanation for the observed similarity could be that most satellites in the considered mass range were recently accreted onto the main halo and acquired a significant fraction of their ex-situ component when they were centrals of other halos.

Figure 4 compares the line-of-sight stellar velocity dispersion profiles for centrals and satellites separately and displays a key result in this paper. Whereas for MaNGA we find that massive centrals and satellites show similar velocity dispersion profiles, in contrast, for the most massive bin we find that TNG100 predicts a $\approx 50\,\mathrm{km\,s^{-1}}$ offset between centrals and satellites. The amount of DM in central simulated galaxies could provide an explanation for the significant difference in velocity dispersion between TNG100 centrals and satellites. As discussed in Lovell et al. (2018), TNG100 predicts an important enhancement of the DM content in the inner regions of subhalos. Hence, this high fraction of DM, that dominates galaxies at $z \approx 0$, may be the responsible of this high velocity dispersion especially for the most massive central galaxies. Our observations appear to exclude a difference in the velocity dispersion profile between centrals and satellites. However, determining whether a galaxy is a central or a satellite is notoriously difficult, and misclassifications in the Yang et al. (2007) catalogue may erase the observational signal. This possibility warrants further investigation before firm conclusions can be drawn.

4.6 Robustness of Results

We now present a discussion on the robustness of the results.

- *Sample matching method* – MaNGA galaxies can be matched to simulated galaxies according to stellar mass or number density. We have tried both and found only minor differences. These are discussed further in Appendix B.

- *Different definitions of stellar masses* – Given the wide variety of possible systematic effects on the definition of stellar masses, in Chapter 3 of Cannarozzo (2021) the same analysis was performed by testing also the SerExp Dust-free stellar masses (from Mendel et al. 2014), the Sérsic and Petrosian fit estimates from the original NSA catalogue, and the masses defined as the sum of the masses included in the 5 concentric annuli used to derive the profiles of stellar properties from FIREFLY and PROSPECTOR for MaNGA ETGs, while for TNG100 galaxies we considered also the stellar masses within a projected aperture of 30 kpc. These tests do not reveal significant differences from the analysis presented in this work.

- *Different definitions of ETGs* – Also the ETG selection is a factor that could affect the results of this study. In Appendix A of Diemer et al. (2019), the authors compare the ETG fractions derived from diverse selection methods in IllustrisTNG with that from the observed compilation of Calette et al. (2018). In particular, the authors measure the ETG fractions adopting classifications based on the concentration of the 3D stellar mass density profiles, C_{82}, defined as $5 \times \log(r_{80}/r_{20})$, with r_{80} and r_{20} as the radii including the 80% and 20% of the total stellar mass, on $(g-r)$ colours, on spheroid-to-total ratios S/T, and on the fraction of kinetic energy that is in rotation κ_{rot}. They found that the best indicator of galaxy morphology able to better reproduce the to reproduce the ETG fraction from Calette et al. (2018) is C_{82}. Instead, the $(g-r)$ classification implies an excess of ETGs, and that the colours correlate weakly with structural parameters (as illustrated also in Rodriguez-Gomez et al. 2019). Tacchella et al. (2019) studied the connection between the star formation activity and morphology of central galaxies in IllustrisTNG, adopting as morphological indicators the parameters C_{82} and S/T. They found that the S/T parameter strongly correlates with $(g-r)$ colours: S/T is higher for redder colours and higher stellar masses (while, at fixed mass, C_{82} is found to be weakly dependent on colour). Our choice of adopting a simple selection on colours is driven by the fact that mock colours in IllustrisTNG are generated consistently with observations (we remind that these mock colours are obtained following the observational prescriptions described in section 3 of Nelson et al. 2018). As done for the different stellar mass definitions, in Chapter 3 of Cannarozzo (2021) we adopted another ETG selection for both the MaNGA and TNG100 samples, including only those objects with SFRs below 1 dex from the star-forming main sequence of galaxies (one of the methods to select passive systems presented in Donnari et al. 2019). Based on

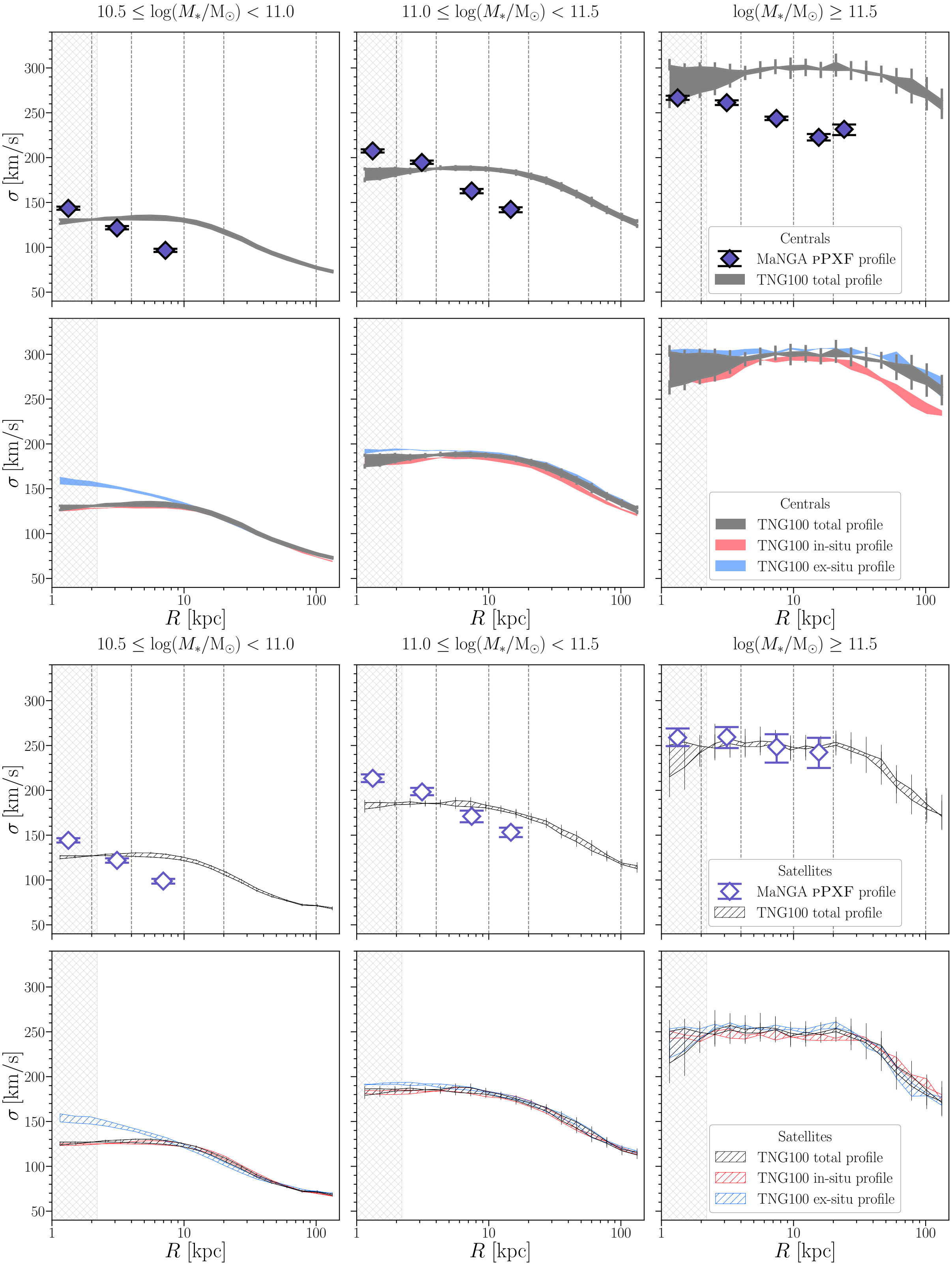

Figure 4. Line-of-sight stellar velocity dispersion radial profiles for centrals (upper rows) and satellites (lower rows). The violet-filled black and white-filled violet diamonds represent the median estimates of the mass-weighted velocity dispersion profiles for MaNGA central and satellite ETGs from pPXF code, respectively. The vertical grey dashed lines delimit the 5 radial intervals within stellar velocity dispersion is computed for MaNGA ETGs. The shaded and hatched areas represent the regions delimited by the median values of the mass-weighted velocity dispersion profiles obtained from the original TNG100 maps and the maps convolved with the MaNGA PSF for centrals and satellites, respectively. Black, red and blue colours correspond to the total, in-situ, and ex-situ stellar populations. For clarity reasons, we show only the errobars for the MaNGA and TNG100 total stellar population profiles. The light grey hatched area ($R \lesssim 2.1$ kpc) shows three times the gravitational softening length of the stellar particles in TNG100.

this extensive exploration, even the results here presented are robust and independent of the specific definitions of ETGs for both the observed and simulated sources.

As mentioned above, the selection of ETGs may involve different criteria, each of which may introduce some selection biases (see also Moresco et al. 2013). Usually, ETGs are characterised by either an elliptical (E) or a lenticular (S0) morphology. One of the historical criteria for morphological selection of galaxies is that based on the T-Type (de Vaucouleurs 1959). According to the T-Type-based classification, E/S0 galaxies have values between −6 and −1, while the various types of spiral galaxies range between 0 and 9. In light of that, for MaNGA objects we also verified the impact of the adopted selection based on colours (see subsection 2.3), checking the morphological type assigned by the MaNGA Morphology Deep Learning DR15 catalog[17]. This catalogue, presented in Fischer et al. (2019), is built by exploiting the Deep Learning method for identifying the morphology of galaxies as described in Domínguez Sánchez et al. (2020) for all the objects of MaNGA DR15. In our Red Galaxy sample, ≈ 66% of the total effectively shows a clear morphology compatible with an E/S0 type, of which ≈ 33% are classified as lenticular galaxies.

5 DISCUSSION

In this section we discuss our results and compare our findings with previous works.

5.1 The role of mergers in TNG100 galaxies

Figure 3 shows that the shapes of the in-situ and ex-situ stellar mass surface density radial profiles from TNG100 ETGs are stellar-mass dependent and that the ex-situ component dominates the total profile at all radii above $\log(M_*/\mathrm{M}_\odot) \approx 11$. This agrees with previous results from Pillepich et al. (2018b), Tacchella et al. (2019), and Pulsoni et al. (2021), who find that the stellar mass assembly history of very massive galaxies is driven by major mergers. Indeed, major mergers not only allow ex-situ stellar populations to settle even in the innermost regions of galaxies, but also homogeneously mix the two stellar components at all radii, causing the formation of stellar mass surface density profiles which are similar in shape and differ only in their normalisation. However, the results of IllustrisTNG disagree with some previous works finding that the growth of massive ETGs is primarily driven by minor mergers. (e.g., Naab et al. 2009; Oser et al. 2010; Hilz et al. 2013). For example, as argued in Genel et al. (2008), and in Khochfar & Silk (2009), massive ($\gtrsim 10^{11}\,\mathrm{M}_\odot$) DM halos undergo typically no more than one major merger in the redshift range $0 \lesssim z \lesssim 2$. There aro also some observational works supporting the idea that massive ETGs may experience few major mergers (e.g., Bell et al. 2006; McIntosh et al. 2008), instead undergoing a high number of minor mergers (e.g., Bundy et al. 2009). On the contrary, other studies lends support to the idea in which the role of major mergers may be more relevant, estimating relatively high mass-weighted merger ratios. For example, Sonnenfeld et al. (2017) infer for galaxies of $\log(M_*/\mathrm{M}_\odot) \approx 11$ a mass-weighted merger ratio greater than 0.4.

Figure 5 displays how minor and major mergers contribute to the the total mass of TNG100 ETGs as a function of redshift and galaxy mass. For each stellar mass bin, the data distributions are presented as *violin plots* (except for the number of mergers), which displays the probability density of the data smoothed by a kernel density estimator. The shape of each violin plot represents the frequency of data, so that the larger the violin's body, the higher the density of data at a given y-axis value. Specifically, we make use of 100 data points to evaluate each Gaussian kernel density estimation. The complementary behaviour of the in-situ and ex-situ stellar mass fractions in the top-left panel of Figure 5 confirms the rising importance of accreted stars in higher-mass ETGs. In particular, the median of the ex-situ stellar fraction grows from ≈ 29% for galaxies with $10.5 \le \log(M_*/\mathrm{M}_\odot) < 11$, up to ≈ 77% for the most massive systems. Following Rodriguez-Gomez et al. (2015, 2016), μ_* is defined as the *stellar mass ratio* between the two progenitors of a given galaxy. A *major merger* is then defined by a $\mu_* > 1/4$, while a *minor merger* is defined by $1/10 < \mu_* < 1/4$. However, the fraction of accreted stars from other galaxies is not only due to major and minor mergers. It also includes stars from the so-called *very minor mergers*, i.e. with $\mu_* < 1/10$, as well as tidally stripped stars from surviving galaxies. As illustrated in the top-right panel of Figure 5, the analysis of the ex-situ fraction accreted via minor mergers relative to the total ex-situ fraction, reveals that, on average, around 6% of stars are accreted via minor mergers in ETGs with $M_* < 10^{11}\,\mathrm{M}_\odot$, reaching ≈ 14% in the most massive galaxies. By isolating the role of major mergers, their contribution presents broad distributions, with median values of around 50% (relative to the whole ex-situ stellar fraction) for ETGs with $\log(M_*/\mathrm{M}_\odot) > 11$. The analysis of the relative contributions deriving from both minor and major mergers suggests that, on average, below $10^{11}\,\mathrm{M}_\odot$, TNG100 galaxies accrete the majority of their ex-situ stellar population through very minor mergers and by stripping stars from surviving objects. Indeed, for these systems $(f_{\text{ex-situ, minor merger}} + f_{\text{ex-situ, major merger}})/f_{\text{ex-situ}} \approx 39\%$. Instead, above $10^{11}\,\mathrm{M}_\odot$, more than 60% of the ex-situ component comes from minor and major mergers, with a larger contribution from major mergers. Considering the distributions of the number of minor and major mergers in TNG100 ETGs for galaxies below $10^{11}\,\mathrm{M}_\odot$ over the redshift range $0.1 \le z \le 2$, below $10^{11}\,\mathrm{M}_\odot$, ETGs usually undergo at most one minor and/or major mergers, while above $10^{11}\,\mathrm{M}_\odot$ the distributions are slightly wider, confirming the important role of major mergers in shaping massive galaxies. Finally, TNG100 ETGs experience, on average, their last major mergers slightly more recently than their last minor mergers. However, we stress here that by minor mergers we refer to systems with $1/10 < \mu_* < 1/4$, which excludes the very minor mergers (i.e. $\mu_* < 1/10$). In addition, we draw attention to the fact that, at a given stellar mass, both the distributions and their median values of the last minor and major mergers are similar, implying that the differences are fairly small. The difference between the median values for the same subsample are lower than 1 Gyr.

5.2 Comparison with Recent Works

In section 4, we discussed the comparison of the circularised radial distributions of the stellar mass surface density, metallicity, age, and velocity dispersion between in MaNGA and TNG100 ETGs. In this section, we compare our results with other works from the literature.

Using a sample of 366 ETGs with masses in the range $9.9 < \log(M_*/\mathrm{M}_\odot) < 10.8$ selected via the the Galaxy Zoo mor-

---

[17] Available at `https://www.sdss.org/dr15/data_access/value-added-catalogs/?vac_id=manga-morphology-deep-learning-dr15-catalogue`

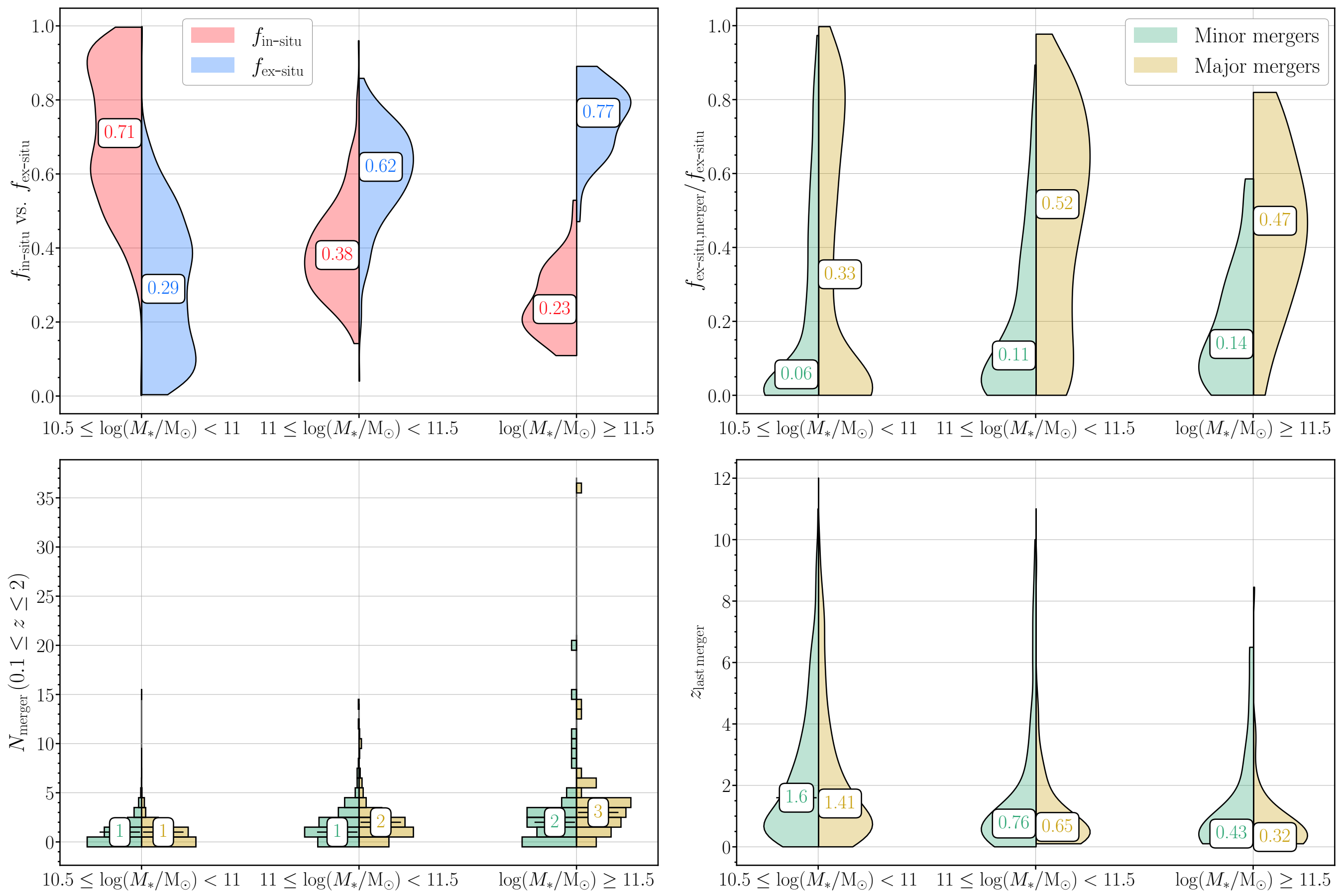

Figure 5. Data distributions of eight properties related to the merger histories of TNG100 ETGs. Top-left panel: total fractions of the in-situ (red distributions) and the ex-situ (blue distributions) stellar components. Top-right panel: fractions of the ex-situ stellar component from minor (green) and major (ocre) mergers normalised to the total ex-situ stellar fraction. Bottom-left panel: number of minor (green) and major (ocre) mergers across the redshift range $0.1 \le z \le 2$. Bottom-right panel: redshifts of the last minor (green) and major (ocre) mergers. All distributions are shown for the same three stellar mass bins as in Figure 2 and in Figure 3. Except for the number of minor and major mergers which are discrete values, the other properties are displayed as violin plots. For each property, the median value of the corresponding distribution is reported.

phological classification (Lintott et al. 2011; Willett et al. 2013), plus visual inspection, Parikh et al. (2018, 2019) analysed the radial gradients of stellar age and metallicity out to one effective radius. If we consider in our sample only galaxies with stellar mass lower than $10^{10.8}$ $\text{M}_\odot$ and we rescale our profiles in units of R_e (the median R_e for our MaNGA ETGs with stellar mass lower than $10^{10.8}$ is $\lesssim 3$ kpc) to directly compare the results with those from Parikh et al. (2018, 2019), we find a satisfying consistency with their stellar age and metallicity radial distributions.

Bernardi et al. (2019) show stellar population gradients for a sample of MaNGA DR15 ETGs subdivided into slow and fast rotators. These ETGs are identified as in Domínguez Sánchez et al. (2020), i.e. applying a morphological classification based on T-Type ≤ 0 (see also subsection 2.4), considering both pure ellipticals and lenticulars. The stellar age and metallicity gradients measured by Bernardi et al. (2019) out to $1\,R_\text{e}$ are qualitatively compatible with our estimates. One of the most relevant outcomes of Bernardi et al. (2019) is that slow rotators dominate above $\log(M_*/\text{M}_\odot) \approx 11.5$: at this stellar mass, where also the size-mass relation slope changes (see Bernardi et al. 2011), the majority of these ellipticals are central galaxies[18]. As an extension of the Bernardi et al. (2019) work, Domínguez Sánchez et al. (2020) focus on stellar properties of S0 lenticular galaxies, highlighting a bimodality in this galaxy population that depends on stellar mass. Above $\log(M_*/\text{M}_\odot) \approx 10.5$, indeed, these galaxies are characterised by stronger age and velocity dispersion gradients, with, instead, negligible gradients in metallicity.

Recently, Barrera-Ballesteros et al. (2022) analysed the entire set of around 10000 galaxies from the MaNGA survey, presenting the radial distributions of several physical properties, selecting in particular a subset of about 1400 sources with optimal spatial coverage, for which the authors studied the impact of a selection based on either stellar mass or morphology. Among the properties derived through the the newest pyPipe3D pipeline (Sánchez et al. 2022), the authors measured the radial distributions of stellar mass surface density, luminosity-weighted stellar metallicity and age, and velocity dispersion. The negative gradients found from Barrera-Ballesteros et al. (2022) for the stellar mass surface density and metallicity in elliptical and lenticular galaxies are qualitatively in agreement with the measurements obtained in this manuscript, reflecting also the

---

[18] Bernardi et al. (2019) make use of the Yang et al. (2007) environmental catalogue used also in this work.

increasing of the normalisations of both profiles as the stellar mass goes up. Even the velocity dispersion profiles agree with those computed by pPXF, finding decreasing distributions towards the outer regions, and central measurements of $\sim 150\,\mathrm{km\,s^{-1}}$ for E/S0 galaxies with $10.5 < \log(M_*/\mathrm{M}_\odot) < 11$, and of $\sim 250\,\mathrm{km\,s^{-1}}$ for objects with $\log(M_*/\mathrm{M}_\odot) > 11$, similarly to those presented here. Regarding stellar ages, the profiles in Barrera-Ballesteros et al. (2022) show values slightly more consistent with those derived by Prospector (i.e., $\gtrsim$ 9 Gyr) presented in this paper, though their radial distributions tend to reduce at large distances, implying the presence of younger stellar populations in the outer regions of galaxies. Also Oyarzún et al. (2022) present the radial profiles for stellar mass surface density from Prospector, as well as for element abundances (i.e. [Fe/H] and [Mg/Fe]) and ages from alf (Conroy et al. 2018; Conroy & van Dokkum 2012; see also Conroy et al. 2014; Choi et al. 2014) for a subset of about 2200 passive centrals from MaNGA to understand the impact of stellar and halo masses in assembling these systems. The radial distributions of stellar mass surface density and [Fe/H] (that we can consider as a measurement of the stellar metallicity) are consistent with those shown in Figure 2. The ages provided by alf, on average, lie in between our measurements from FIREFLY and Prospector, showing also the presence of younger stellar populations in the inner regions.

Using the results from the Illustris simulation, Cook et al. (2016) investigated the stellar population gradients for a sample of more than 500 ETGs with $10 \leq \log(M_*/\mathrm{M}_\odot) \leq 12$. The stellar surface brightness, metallicity, and age gradients are overall in agreement with observables. The gradients are subdivided into three intervals: the inner galaxy ($0.1{-}1\,R_\mathrm{e}$), the outer galaxy ($1{-}2\,R_\mathrm{e}$), and the stellar halo ($2{-}4\,R_\mathrm{e}$). Except for the age gradients which are found to be not so informative about the accretion histories of galaxies, both the surface-brightness and metallicity profiles show that, at fixed stellar mass, the ex-situ stellar component produce flatter profiles. In particular, as the stellar mas increases, the higher the accreted star fraction, the flatter the profiles. Though the flattening at large radii of the stellar mass surface density and metallicity profiles is not apparent in Figure 2, because of the adopted logarithmic scale, we verified that our profiles are quantitatively consistent with those of Cook et al. (2016) when a linear scale in units of R_e is adopted. Albeit a qualitative agreement in the behaviour of radial profiles is found using Illustris and IllustrisTNG, the fraction of accreted stars as well as the role of mergers in shaping galaxies are significantly different. As highlighted in Figure 10 of Tacchella et al. (2019), though in both simulations the fraction of ex-situ stars at $z = 0$ rapidly increases above $10^{10.5}\,\mathrm{M}_\odot$, TNG100 predicts a fraction that, on average, is higher by a factor of $\approx 30\%$ with respect to the total stellar amount. Moreover, while the main channel for the stellar accretion in Illustris is via minor mergers, as shown in the top-right panel of Figure 5, TNG100 predicts a more relevant role of major mergers. These two substantial differences between Illustris and IllustrisTNG are primarily due to the diverse feedback model implemented and the consequent stellar mass functions. In a more recent work, Pulsoni et al. (2020) studied the photometric and kinematic properties out to 15 R_e of ETGs stellar halos for 1114 objects in TNG100 (together with other 80 sources in TNG50), with stellar masses $10.3 < \log(M_*/\mathrm{M}_\odot) < 12$ and selected in $(g - r)$ colours (similarly with the selection adopted in this paper) and in the angular momentum–ellipticity plane. Analogously to our findings, the high-mass tail of ETGs are everywhere dominated by the accreted stellar component, mainly acquired through major mergers. In addition, IllustrisTNG ETGs are compared with some observational surveys, including MaNGA galaxies. Looking at the distribution of galaxies in the angular momentum–ellipticity plane within 1 R_e, a percentage of the IllustrisTNG galaxies lie in a region where no observed ETGs are found: these are basically elongated, triaxial systems. However, when simulated galaxies with an intermediate-to-major axis ratio < 0.6 at 1 R_e are removed - the centrally elongated objects -, these ETGs reflect the location in the plane of the observed counterpart, except for a region where a large fraction of MaNGA S0 have a high angular momentum.

Overall, the results presented in this manuscript are generally in agreement with previous works in the literature. In particular, the distributions of the stellar properties for the observed galaxies analysed in this work confirm the common trend of negative gradients for stellar mass surface density, metallicity, and velocity dispersion, whose normalisations increase as the stellar mass increases. The radial distributions of stellar age, however, are not always in agreement with those presented in previous works. The differences, whether in normalisation or in shape, may depend on multiple factors, such as the considered samples or the stellar fitting codes and libraries used to estimate the age of stellar populations. The scope of this work is to outline a possible scenario for the merger-driven evolution of observed ETGs in the present-day Universe. The scenario predicted by IllustrisTNG in which major mergers may be crucial in shaping massive galaxies at $z \approx 0$ is somewhat in contrast with some previous theoretical findings (e.g., Naab et al. 2009; Oser et al. 2010; Hilz et al. 2013) which, conversely, back an evolution mainly driven by a high number of minor mergers.

6 SUMMARY AND CONCLUSIONS

In this paper we studied the radial profiles of stellar mass surface density, metallicity, age, and line-of-sight velocity dispersion in massive ($M_* \geq 10^{10.5}\,\mathrm{M}_\odot$) ETGs, selected in colours with $(g - r) > 0.6$, comparing observed galaxies from the MaNGA DR15 survey with simulated galaxies from TNG100 of the IllustrisTNG magneto-hydrodynamical cosmological simulation suite. For both galaxy samples, the stellar property profiles have been obtained building concentric elliptical annuli on the bi-dimensional projected maps of each source, disentangling in TNG100 ETGs the in-situ and ex-situ stellar populations, and both accounting or not accounting for the effects of convolving the maps by MaNGA PSF. All the presented stellar population properties are at face value, i.e. the measurements are directly obtained from pipelines and stellar fitting codes for MaNGA, and from the simulation for TNG100 ETGs.

Our main results are the following.

- We find a satisfying agreement between observations and simulations in the stacked radial profiles of the stellar mass surface density of massive ETGs, both in shape and normalisation. This agreement is observed at all radii and at all stellar mass bins, and is independent of ETG and stellar mass definitions.
- Overall, TNG100 ETGs have, on average, stellar metallicity and velocity dispersion profiles reasonably similar to those observed in MaNGA ETGs. Concerning metallicity, the shape of MaNGA profiles is well reproduced by TNG100 galaxies, though in some cases the observed and simulated profiles differ in normalisation (around 0.15 dex in the outermost parts of ETGs with $M_* \gtrsim 10^{11.5}\,\mathrm{M}_\odot$). For galaxies $M_* < 10^{11.5}\,\mathrm{M}_\odot$, we find a decent agreement for the radial distributions of velocity dispersion between simulated and observed ETGs, the latter showing steeper profiles that differ at most by $\approx 30\,\mathrm{km\,s^{-1}}$ from the simulated ETG distributions. Only the very massive ($M_* \gtrsim 10^{11.5}\,\mathrm{M}_\odot$) systems of TNG100 tend to have, over the entire explored radial range, higher

velocity dispersion than the corresponding observed system, by up to $\approx 50\,\mathrm{km\,s^{-1}}$.

- The ages of the stellar populations of observed ETGs are highly uncertain, and significantly different age estimates are obtained using different codes (FIREFLY and Prospector, which differ of about 2−2.5 Gyr at all radii and at all stellar mass bins). The age profiles of stellar populations in TNG100 are found to lie in between the profiles estimated for the corresponding observed ETGs with FIREFLY and Prospector.
- By separating central and satellite galaxies for both TNG100 and MaNGA samples, we find that there are not relevant differences in all the profiles between the two galaxy populations, except for the velocity dispersion profiles of massive systems ($M_* > 10^{11.5}\,\mathrm{M_\odot}$, see Figure 4). Indeed, while TNG100 and MaNGA satellites have similar velocity dispersion profiles, central simulated galaxies tend to have velocity dispersion at all radii higher than observed ETGs ($\approx 50\,\mathrm{km\,s^{-1}}$).
- The behaviour of the in-situ and ex-situ surface density profiles identifies two different scenarios for the merger-driven history of these objects, corroborating previous outcomes in the literature, such as from Pillepich et al. (2018b) and Tacchella et al. (2019): galaxies with $M_* \lesssim 10^{11}\,\mathrm{M_\odot}$ are mainly dominated by the in-situ stellar populations out to ≈ 30 kpc; instead, in ETGs with $M_* \gtrsim 10^{11}\,\mathrm{M_\odot}$, the contribution of the ex-situ stars is at least as important as that of the in-situ component, and even totally dominating for very massive ETGs ($M_* \gtrsim 10^{11.5}\,\mathrm{M_\odot}$).
- The similar shapes found for the radial distributions of the stellar mass surface densities for both in-situ and ex-situ stars (see Figure 3) as well as the detailed analysis of the merger history (see Figure 5) in simulated ETGs reveal that especially galaxies with $M_* \gtrsim 10^{11}\,\mathrm{M_\odot}$ experienced across cosmic time an evolution mainly driven by major mergers. Indeed, major mergers allow both to explain the presence of a significant percentage of ex-situ stars that are able to penetrate even in the innermost parts of galaxies, and also that the two stellar components are well homogenised at all radii, showing similar surface density profiles. The results from TNG100 illustrated in this paper and in previous works in literature (e.g., Pillepich et al. 2018b; Tacchella et al. 2019; Pulsoni et al. 2021) support the possible scenario in which massive systems assembled across their cosmic histories mainly via major mergers (see also Sonnenfeld et al. 2017), in contrast with some previous theoretical (e.g., Naab et al. 2009; Oser et al. 2010; Hilz et al. 2013) and observational (e.g., Bell et al. 2006; McIntosh et al. 2008) studies which, instead, endorse a minor merger-driven evolution for ETGs.

For the future, we plan to extend the analysis to other physical properties, like chemical abundances of individual elements. In order to provide a more complete scenario behind the cosmic evolution of the ETGs that we observe in the present-day Universe, in simulations we will study the merger history of individual galaxies, considering the evolution of the spatial distribution of their stellar properties. Finally, we will make use of the newest TNG50 simulation of IllustrisTNG which, though characterised by a smaller physical volume and thus a lower statistics, benefits from a higher mass resolution that could allow us to make a more reliable comparison at smaller scales of galaxies with data from current and upcoming surveys.

ACKNOWLEDGEMENTS

We are grateful to M. Auger and M. Bernardi for helpful pieces of advice and comments, which remarkably enriched the analysis presented in this work. We sincerely thank the referee A. Pillepich for her feedback and suggestions that considerably contributed to improve the quality of this manuscript. CC acknowledges useful discussions with F. Ardila, C. Bacchini, F. Belfiore, C. D'Eugenio, G. Iorio, M. Mingozzi, R. Pascale, S. Quai, and S. Tacchella. This material is based upon work supported by the National Science Foundation under Grant No. 1714610.

DATA AVAILABILITY

The data underlying this article regarding the selection of galaxy samples and the radial profiles will be shared upon request to the corresponding author. IllustrisTNG data are publicly available at `https://www.illustris-project.org/data/` (Nelson et al. 2019a). The MaNGA galaxy sample is drawn from an extended version of the NASA-Sloan Atlas (NSA `v1_0_1`, `https://www.sdss.org/dr15/manga/manga-target-selection/nsa/`; Blanton et al. 2011) catalogue. MaNGA DR15 data are taken from `https://www.sdss.org/dr15/manga/manga-data/` (Aguado et al. 2019). The stellar masses for MaNGA galaxies are included in the UPenn_PhotDec_MsSTAR catalogue (`http://alan-meert-website-aws.s3-website-us-east-1.amazonaws.com/fit_catalog/download/index.html`; Meert et al. 2015). To check the impact of the adopted selection for the MaNGA sample, we relied on the morphological type presented in the MaNGA Morphology Deep Learning DR15 catalog (`https://www.sdss.org/dr15/data_access/value-added-catalogs/?vac_id=manga-morphology-deep-learning-dr15-catalogue`; Fischer et al. 2019).

References

Adelman-McCarthy J. K., et al., 2006, ApJS, 162, 38
Aguado D. S., et al., 2019, ApJS, 240, 23
Aihara H., et al., 2018, PASJ, 70, S8
Alam S., et al., 2015, ApJS, 219, 12
Ardila F., et al., 2021, MNRAS, 500, 432
Bacon R., et al., 2001, MNRAS, 326, 23
Barber C., Schaye J., Crain R. A., 2019, MNRAS, 483, 985
Barrera-Ballesteros J. K., et al., 2022, arXiv e-prints, p. arXiv:2206.07058
Bell E. F., et al., 2006, ApJ, 640, 241
Belli S., Newman A. B., Ellis R. S., 2014, ApJ, 783, 117
Belli S., Newman A. B., Ellis R. S., 2017, ApJ, 834, 18
Bernardi M., Roche N., Shankar F., Sheth R. K., 2011, MNRAS, 412, L6
Bernardi M., Meert A., Sheth R. K., Fischer J. L., Huertas-Company M., Maraston C., Shankar F., Vikram V., 2017, MNRAS, 467, 2217
Bernardi M., Domínguez Sánchez H., Brownstein J. R., Drory N., Sheth R. K., 2019, MNRAS, 489, 5633
Blanton M. R., Kazin E., Muna D., Weaver B. A., Price-Whelan A., 2011, AJ, 142, 31
Blanton M. R., et al., 2017, AJ, 154, 28
Bottrell C., Hani M. H., 2022, MNRAS, 514, 2821
Bryant J. J., et al., 2015, MNRAS, 447, 2857
Bundy K., Fukugita M., Ellis R. S., Targett T. A., Belli S., Kodama T., 2009, ApJ, 697, 1369
Bundy K., et al., 2015, ApJ, 798, 7
Calette A. R., Avila-Reese V., Rodríguez-Puebla A., Hernández-Toledo H., Papastergis E., 2018, Rev. Mex. Astron. Astrofis., 54, 443
Cannarozzo C., 2021, PhD thesis, Alma Mater Studiorum Università di Bologna, `http://amsdottorato.unibo.it/9874/`
Cannarozzo C., Sonnenfeld A., Nipoti C., 2020, MNRAS, 498, 1101
Cappellari M., 2017, MNRAS, 466, 798

Cappellari M., Emsellem E., 2004, PASP, 116, 138
Cappellari M., et al., 2011, MNRAS, 413, 813
Chabrier G., 2003, PASP, 115, 763
Choi J., Conroy C., Moustakas J., Graves G. J., Holden B. P., Brodwin M., Brown M. J. I., van Dokkum P. G., 2014, ApJ, 792, 95
Choi J., Dotter A., Conroy C., Cantiello M., Paxton B., Johnson B. D., 2016, ApJ, 823, 102
Cimatti A., Fraternali F., Nipoti C., 2019, Introduction to galaxy formation and evolution: from primordial gas to present-day galaxies. Cambridge University Press
Comparat J., et al., 2017, arXiv e-prints, p. arXiv:1711.06575
Conroy C., 2013, ARA&A, 51, 393
Conroy C., Gunn J. E., 2010, ApJ, 712, 833
Conroy C., van Dokkum P., 2012, ApJ, 747, 69
Conroy C., Gunn J. E., White M., 2009, ApJ, 699, 486
Conroy C., Graves G. J., van Dokkum P. G., 2014, ApJ, 780, 33
Conroy C., Villaume A., van Dokkum P. G., Lind K., 2018, ApJ, 854, 139
Cook B. A., Conroy C., Pillepich A., Rodriguez-Gomez V., Hernquist L., 2016, ApJ, 833, 158
Crain R. A., et al., 2015, MNRAS, 450, 1937
Croom S. M., et al., 2012, MNRAS, 421, 872
Damjanov I., Zahid H. J., Geller M. J., Utsumi Y., Sohn J., Souchereau H., 2019, ApJ, 872, 91
Davison T. A., Norris M. A., Leaman R., Kuntschner H., Boecker A., van de Ven G., 2021, MNRAS, 507, 3089
de Vaucouleurs G., 1959, Handbuch der Physik, 53, 275
de Zeeuw P. T., et al., 2002, MNRAS, 329, 513
Diemer B., et al., 2018, ApJS, 238, 33
Diemer B., et al., 2019, MNRAS, 487, 1529
Djorgovski S., Davis M., 1987, ApJ, 313, 59
Domínguez Sánchez H., Bernardi M., Nikakhtar F., Margalef-Bentabol B., Sheth R. K., 2020, MNRAS, 495, 2894
Donnari M., et al., 2019, MNRAS, 485, 4817
Dotter A., 2016, ApJS, 222, 8
Dressler A., Lynden-Bell D., Burstein D., Davies R. L., Faber S. M., Terlevich R., Wegner G., 1987, ApJ, 313, 42
Drory N., et al., 2015, AJ, 149, 77
Edwards L. O. V., et al., 2020, MNRAS, 491, 2617
Faber S. M., Jackson R. E., 1976, ApJ, 204, 668
Ferguson H. C., et al., 2004, ApJ, 600, L107
Fischer J. L., Domínguez Sánchez H., Bernardi M., 2019, MNRAS, 483, 2057
Foreman-Mackey D., Hogg D. W., Lang D., Goodman J., 2013, PASP, 125, 306
Gallazzi A., Charlot S., Brinchmann J., White S. D. M., Tremonti C. A., 2005, MNRAS, 362, 41
Genel S., et al., 2008, ApJ, 688, 789
Genel S., et al., 2014, MNRAS, 445, 175
Goddard D., et al., 2017a, MNRAS, 465, 688
Goddard D., et al., 2017b, MNRAS, 466, 4731
Goodman J., Weare J., 2010, Communications in Applied Mathematics and Computational Science, 5, 65
Greene J. E., Janish R., Ma C.-P., McConnell N. J., Blakeslee J. P., Thomas J., Murphy J. D., 2015, ApJ, 807, 11
Greene J. E., et al., 2019, ApJ, 874, 66
Gunn J. E., et al., 2006, AJ, 131, 2332
Hilz M., Naab T., Ostriker J. P., 2013, MNRAS, 429, 2924
Hirschmann M., et al., 2013, MNRAS, 436, 2929
Hirschmann M., Naab T., Ostriker J. P., Forbes D. A., Duc P.-A., Davé R., Oser L., Karabal E., 2015, MNRAS, 449, 528
Huang S., Leauthaud A., Greene J. E., Bundy K., Lin Y.-T., Tanaka M., Miyazaki S., Komiyama Y., 2018, MNRAS, 475, 3348
Johnson B. D., Leja J. L., Conroy C., Speagle J. S., 2019, Prospector: Stellar population inference from spectra and SEDs (ascl:1905.025)
Khochfar S., Silk J., 2009, MNRAS, 397, 506
Kirby E. N., Cohen J. G., Guhathakurta P., Cheng L., Bullock J. S., Gallazzi A., 2013, ApJ, 779, 102
Kobayashi C., 2004, MNRAS, 347, 740
Kormendy J., 1977, ApJ, 218, 333
Kroupa P., 2001, MNRAS, 322, 231
Kuntschner H., et al., 2010, MNRAS, 408, 97
Lackner C. N., Cen R., Ostriker J. P., Joung M. R., 2012, MNRAS, 425, 641
Larson R. B., 1974, MNRAS, 166, 585
Law D. R., et al., 2015, AJ, 150, 19
Law D. R., et al., 2016, AJ, 152, 83
Law D. R., et al., 2021, AJ, 161, 52
Leja J., Johnson B. D., Conroy C., van Dokkum P. G., Byler N., 2017, ApJ, 837, 170
Leja J., Carnall A. C., Johnson B. D., Conroy C., Speagle J. S., 2019, ApJ, 876, 3
Li H., et al., 2018, MNRAS, 476, 1765
Lintott C., et al., 2011, MNRAS, 410, 166
Lovell M. R., et al., 2018, MNRAS, 481, 1950
Ma C.-P., Greene J. E., McConnell N., Janish R., Blakeslee J. P., Thomas J., Murphy J. D., 2014, ApJ, 795, 158
Maraston C., Strömbäck G., 2011, MNRAS, 418, 2785
Maraston C., et al., 2020, MNRAS, 496, 2962
Marinacci F., et al., 2018, MNRAS, 480, 5113
McAlpine S., et al., 2016, Astronomy and Computing, 15, 72
McIntosh D. H., Guo Y., Hertzberg J., Katz N., Mo H. J., van den Bosch F. C., Yang X., 2008, MNRAS, 388, 1537
Meert A., Vikram V., Bernardi M., 2015, MNRAS, 446, 3943
Mendel J. T., Simard L., Palmer M., Ellison S. L., Patton D. R., 2014, ApJS, 210, 3
Miyazaki S., et al., 2018, PASJ, 70, S1
Moresco M., et al., 2013, A&A, 558, A61
Naab T., Johansson P. H., Ostriker J. P., 2009, ApJ, 699, L178
Naiman J. P., et al., 2018, MNRAS, 477, 1206
Nanni L., et al., 2022, MNRAS,
Nelson D., et al., 2018, MNRAS, 475, 624
Nelson D., et al., 2019a, Computational Astrophysics and Cosmology, 6, 2
Nelson D., et al., 2019b, MNRAS, 490, 3234
Nipoti C., Cannarozzo C., Calura F., Sonnenfeld A., Treu T., 2020, MNRAS, 499, 559
Nipoti C., Cherchi G., Iorio G., Calura F., 2021, MNRAS, 503, 4221
Oser L., Ostriker J. P., Naab T., Johansson P. H., Burkert A., 2010, ApJ, 725, 2312
Oser L., Naab T., Ostriker J. P., Johansson P. H., 2012, ApJ, 744, 63
Oyarzún G. A., et al., 2019, ApJ, 880, 111
Oyarzún G. A., et al., 2022, ApJ, 933, 88
Parikh T., et al., 2018, MNRAS, 477, 3954
Parikh T., et al., 2019, MNRAS, 483, 3420
Pillepich A., et al., 2014, MNRAS, 444, 237
Pillepich A., et al., 2018a, MNRAS, 473, 4077
Pillepich A., et al., 2018b, MNRAS, 475, 648
Pillepich A., et al., 2019, MNRAS, 490, 3196
Pipino A., D'Ercole A., Chiappini C., Matteucci F., 2010, MNRAS, 407, 1347
Planck Collaboration et al., 2016, A&A, 594, A13
Pulsoni C., Gerhard O., Arnaboldi M., Pillepich A., Nelson D., Hernquist L., Springel V., 2020, A&A, 641, A60
Pulsoni C., Gerhard O., Arnaboldi M., Pillepich A., Rodriguez-Gomez V., Nelson D., Hernquist L., Springel V., 2021, A&A, 647, A95
Rodriguez-Gomez V., et al., 2015, MNRAS, 449, 49
Rodriguez-Gomez V., et al., 2016, MNRAS, 458, 2371
Rodriguez-Gomez V., et al., 2019, MNRAS, 483, 4140
Sánchez-Blázquez P., et al., 2006, MNRAS, 371, 703
Sánchez S. F., et al., 2016, A&A, 594, A36
Sánchez S. F., et al., 2022, arXiv e-prints, p. arXiv:2206.07062
Santucci G., et al., 2020, ApJ, 896, 75
Schaye J., et al., 2015, MNRAS, 446, 521
Sijacki D., Vogelsberger M., Genel S., Springel V., Torrey P., Snyder G. F., Nelson D., Hernquist L., 2015, MNRAS, 452, 575
Smee S. A., et al., 2013, AJ, 146, 32
Sonnenfeld A., Nipoti C., Treu T., 2017, MNRAS, 465, 2397
Sonnenfeld A., Wang W., Bahcall N., 2019, A&A, 622, A30

Speagle J. S., 2020, MNRAS, 493, 3132
Springel V., 2010, MNRAS, 401, 791
Springel V., White S. D. M., Tormen G., Kauffmann G., 2001, MNRAS, 328, 726
Springel V., et al., 2018, MNRAS, 475, 676
Tacchella S., et al., 2019, MNRAS, 487, 5416
Tanaka M., et al., 2019, ApJ, 885, L34
Taylor P., Kobayashi C., 2017, MNRAS, 471, 3856
Thomas D., Maraston C., Bender R., Mendes de Oliveira C., 2005, ApJ, 621, 673
van de Sande J., et al., 2013, ApJ, 771, 85
van der Wel A., et al., 2014, ApJ, 788, 28
Vazdekis A., Sánchez-Blázquez P., Falcón-Barroso J., Cenarro A. J., Beasley M. A., Cardiel N., Gorgas J., Peletier R. F., 2010, MNRAS, 404, 1639
Vogelsberger M., et al., 2014a, MNRAS, 444, 1518
Vogelsberger M., et al., 2014b, Nature, 509, 177
Wake D. A., et al., 2017, AJ, 154, 86
Weinberger R., et al., 2017, MNRAS, 465, 3291
Westfall K. B., et al., 2019, AJ, 158, 231
Wilkinson D. M., Maraston C., Goddard D., Thomas D., Parikh T., 2017, MNRAS, 472, 4297
Willett K. W., et al., 2013, MNRAS, 435, 2835
Woo J., Courteau S., Dekel A., 2008, MNRAS, 390, 1453
Worthey G., 1994, ApJS, 95, 107
Yan R., et al., 2016a, AJ, 151, 8
Yan R., et al., 2016b, AJ, 152, 197
Yang X., Mo H. J., van den Bosch F. C., Pasquali A., Li C., Barden M., 2007, ApJ, 671, 153
York D. G., et al., 2000, AJ, 120, 1579
Zheng Z., et al., 2017, MNRAS, 465, 4572

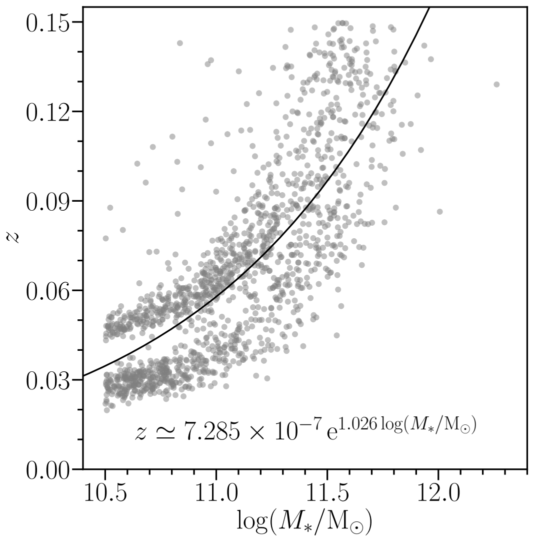

Figure A1. The redshift−stellar mass distributions of the MaNGA ETG sample. The black solid curve traces the fit of the distribution. The corresponding fit functional form is reported. The two stripes of dots trace the Primary sample (the lower cloud) and the Secondary sample (the upper cloud) of the MaNGA sample.

APPENDIX A: COMPUTING THE ANGULAR DIAMETER DISTANCES TO CONVOLVE TNG100 MAPS

As described in subsection 3.2, in order to account for the effects of the MaNGA resolution on simulated galaxies, for each stellar property we consider two limit-case profiles: for a given simulated ETG, one profile is computed directly from the original 2D stellar property map, i.e. the *unconvolved profile*, while the other profile is derived from a map previously convolved with a 2D Gaussian filter kernel σ_{kernel}, i.e. the *convolved profile*. To compute the kernel of each simulated ETG, we use Equation 1, where $\mathcal{R}_{\mathrm{TNG}} = 1$ kpc is the TNG100 resolution of the original maps, while $\mathcal{R}_{\mathrm{MaNGA},i} = \sin(\mathrm{PSF}_{\mathrm{MaNGA}})d_{A,i}$ is the resolution that the i-th TNG100 ETG map should have if it were observed as a MaNGA galaxy, and depends on $\mathrm{PSF}_{\mathrm{MaNGA}} = 2.5''$ and the angular diameter distance $d_{A,i}$ of the i-th TNG100 galaxy. To measure $d_{A,i}$ we rely on the `angular_diameter_distance` function of the Python package Astropy, that takes in input the redshift of the i-th source.

Since MaNGA was built in such a way that the most massive galaxies are located at higher redshifts, we fit the z−M_* distribution of the MaNGA sample considered and we assign to each simulated galaxy the corresponding redshift value depending on its stellar mass. The functional form adopted for fitting the z−M_* distributions in MaNGA is

$$z = a\, e^{b \log(M_*/\mathrm{M}_\odot)}, \tag{A1}$$

where a and b are the two parameters used for the fit. In Figure A1, the z−M_* scatter distributions with the corresponding fit are shown. Thus, the fit is used to assign redshifts to the simulated ETGs to compute their angular diameter distance, and then the kernel used to convolve their stellar property maps. We remind the reader that simulated galaxies are extracted from the $z = 0.1$ snapshot of TNG100-1. However, to make the comparison with MaNGA as fair as possible, for our scope, we ignore this information for convolving the maps and we reassign to each simulated ETG a new redshift corresponding to its stellar mass according to the fit of the MaNGA distribution on the z−M_* plane.

APPENDIX B: COMPARING PROFILES IN NUMBER-DENSITY-BASED STELLAR MASS BINS

In section 4 we presented the radial profiles of MaNGA and TNG100 ETG stellar properties in the three stellar mass bins $10.5 \le \log(M_*/\mathrm{M}_\odot) < 11$, $11 \le \log(M_*/\mathrm{M}_\odot) < 11.5$, and $\log(M_*/\mathrm{M}_\odot) \ge 11.5$. We repeated here the same analysis building stellar mass bins at *fixed number density*. Specifically, we compute the stellar mass function (SMF) for our TNG100 galaxy sample, whereas for MaNGA we use Table 1 of Bernardi et al. (2017) and adopt the observed (i.e. error-broadened) SMF associated with the Dusty ($\mathbf{\Phi}^{\mathrm{M14_d}}_{\mathrm{Obs}}$) mass estimates from Mendel et al. (2014) with the SerExp photometry of Meert et al. (2015). These are the same stellar masses as used for our MaNGA ETGs. Thus, we compute the cumulative stellar mass functions (CSMFs) for both MaNGA and TNG100 as the sum of the number counts of galaxies with stellar masses greater than a given value $M_{*,i}$:

$$n(> M_{*,i}) = \int_{M_{*,i}}^{+\infty} \mathbf{\Phi}(M'_*)\, \mathrm{d}M'_*. \tag{B1}$$

Figure B1 shows the CSMFs for TNG100 and MaNGA samples. We adopt three bins in number density as listed in Table B1. Number density bins could be more robust against possible mismatches in the stellar mass measurements between observations and simulations. Table B1 indicates the values of the stellar masses in both TNG100 and MaNGA samples that correspond to our three number density bins: $-3.50 < \log(n/\mathrm{Mpc}^{-3}) \le -2.75$, $-4.25 < \log(n/\mathrm{Mpc}^{-3}) \le -3.50$, and $\log(n/\mathrm{Mpc}^{-3}) \le -4.25$. The bounds of the number density bins,

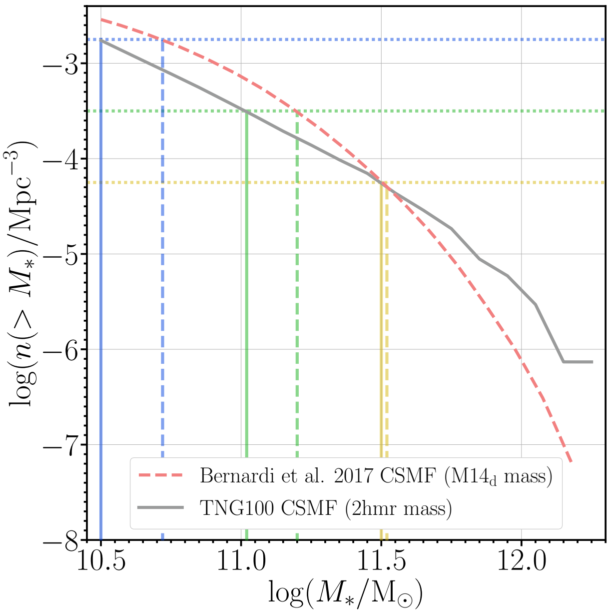

Figure B1. CSMFs for the TNG100 (grey solid curve) and the MaNGA (red dashed curve) samples. Horizontal dotted lines indicate out number-density-based bins: $\log(n/\mathrm{Mpc}^{-3}) = -2.75$ (blue), $\log(n/\mathrm{Mpc}^{-3}) = -3.50$ (green), $\log(n/\mathrm{Mpc}^{-3}) = -4.75$ (yellow). Vertical lines indicate the corresponding stellar mass values for TNG100 (solid lines) and for MaNGA (dashed lines).

Table B1. Stellar mass values corresponding to the bounds of the number density bins. Column 1: number density. Column 2: stellar mass for the MaNGA sample. Column 3: stellar mass for the TNG100 sample. Stellar masses are in units of $\mathrm{M}_\odot$.

$\log(n/\mathrm{Mpc}^{-3})$	$\log M_{*,\mathrm{MaNGA}}$	$\log M_{*,\mathrm{TNG}}$
−2.75	10.72	10.50
−3.50	11.20	11.02
−4.25	11.52	11.50

listed in Table B1, are such that the corresponding stellar mass values for simulated ETGs, i.e. $\log(M_*/\mathrm{M}_\odot) = 10.5, 11.02, 11.5$, almost coincide with the values of stellar masses used in section 4.

As illustrated in Figure B2, the most evident exceptions of adopting the number-density-based stellar mass bins concern the first two bins of the stellar properties analysed. In particular, the discrepancy between the radial profiles of the stellar mass surface density for the observed and simulated ETGs increases, highlighting a tendency of the MaNGA sources to assume slightly higher values, with respect to those shown in Figure 2. A similar behaviour, but less significant, is also found for the stellar metallicity and age distributions. Instead, concerning velocity dispersion, in the first two bins the MaNGA profiles are systematically shifted up by a factor of around 20−30 $\mathrm{km\,s}^{-1}$ All these discrepancies are caused by the fact that, by removing from the MaNGA sample ETGs with $\log M_* \leq 10.78$ in the first bin, and considering galaxies with $\log(M_*/\mathrm{M}_\odot) > 11.2$ in the second bin, the median profiles of the observed sources tend to assume higher values than the counterparts presented in Figure 2.

Since we expect number density bins to more closely approximate a halo-mass-based comparison, the aforementioned differences could be an indication of a mismatch between MaNGA and TNG100 in the stellar-to-halo mass relation. However, qualitatively speaking, the selection in number density bins does not affect remarkably the overall fashion of the profiles for all the stellar properties, showing similar radial distributions as those illustrated in Figure 3.

This paper has been typeset from a TEX/LATEX file prepared by the author.

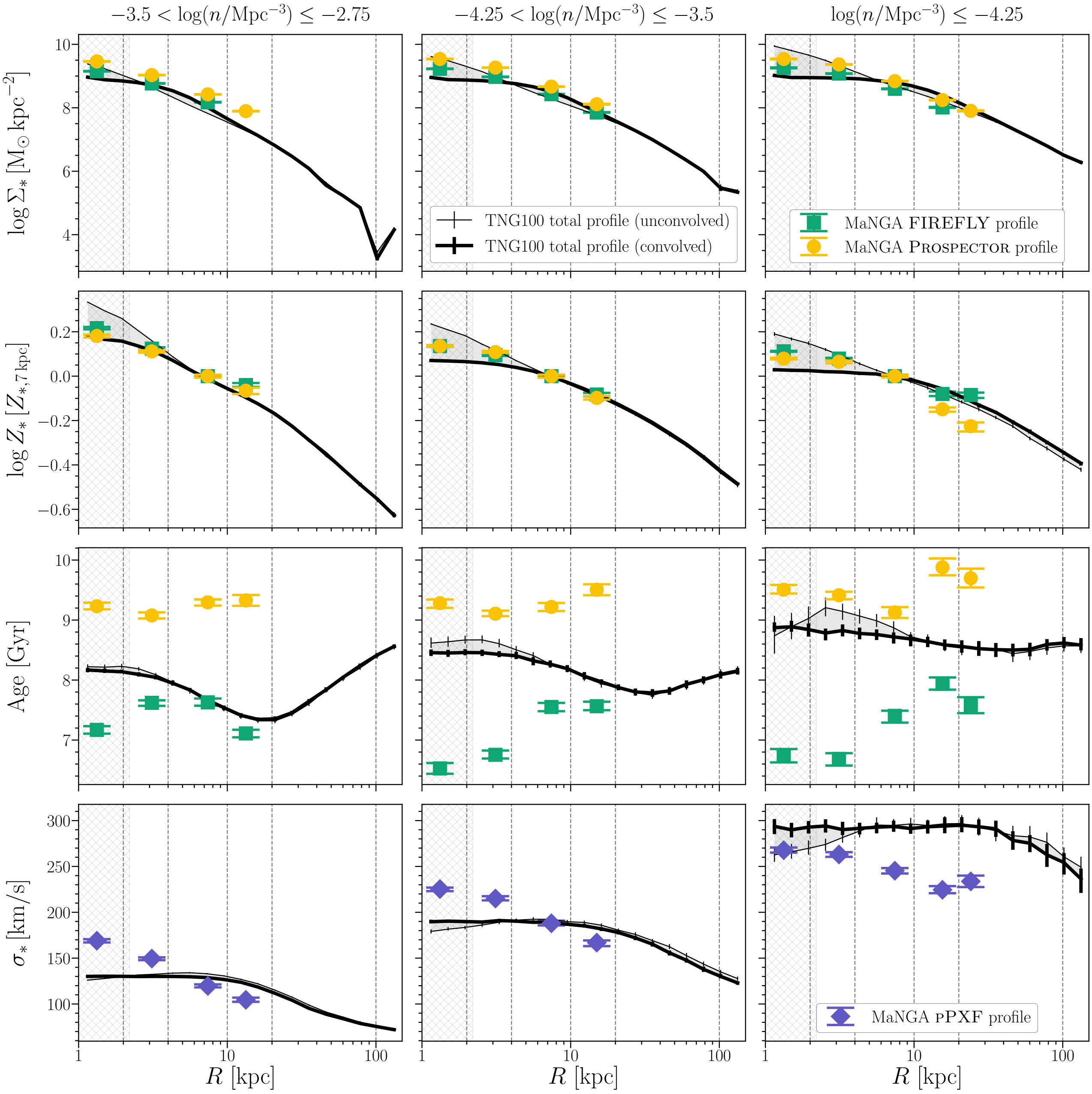

Figure B2. Same as Figure 2, but in number-density-based stellar mass bins.

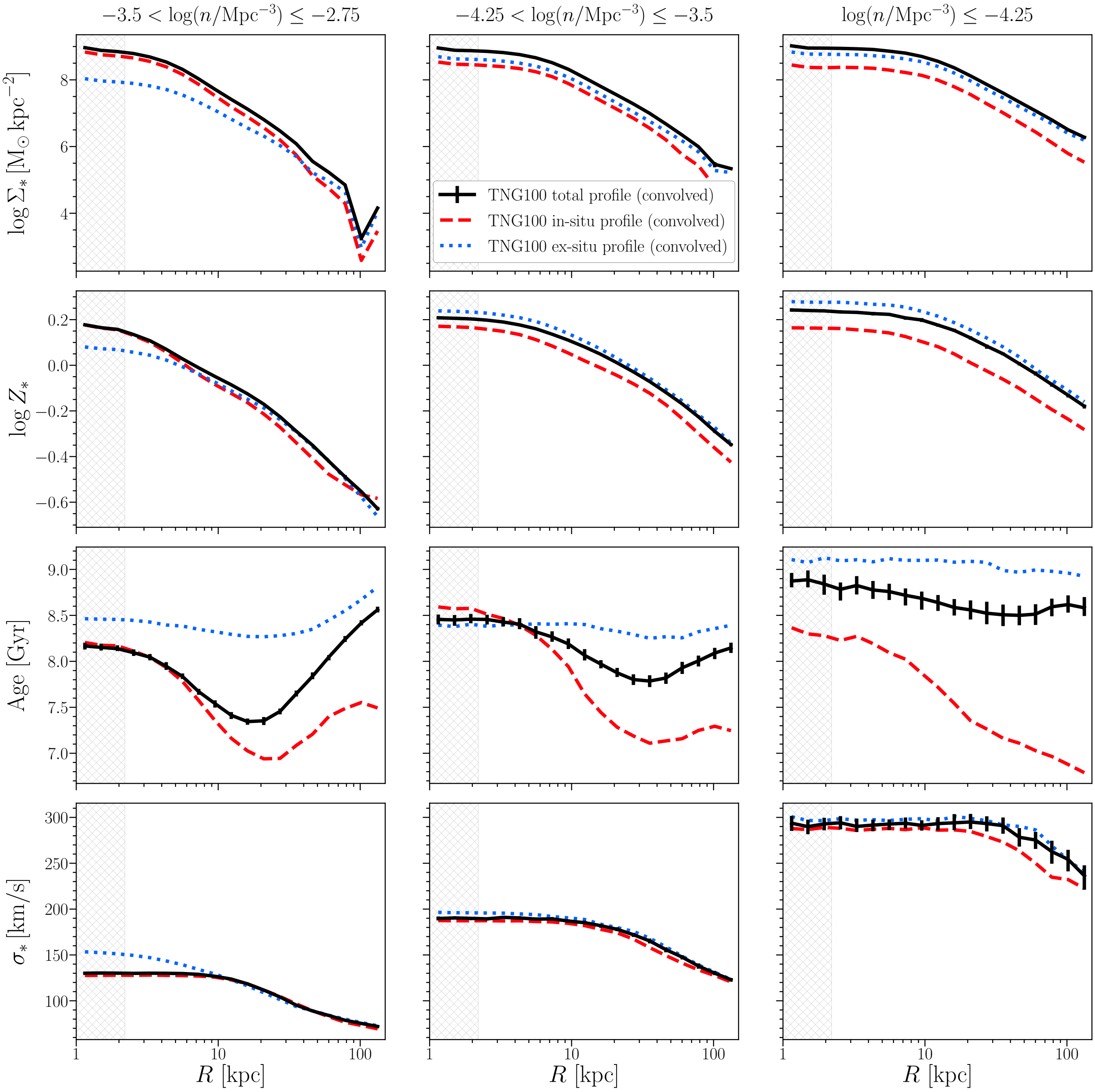

Figure B3. Same as Figure 3, but in number-density-based stellar mass bins.